Conductance Model for Extreme Events : Impact of Auroral Conductance on Space Weather Forecasts

Agnit Mukhopadhyay[1], Daniel T Welling[2], Michael W. Liemohn[3], Aaron J. Ridley[3], Shibaji Chakraborty[4], and Brian J. Anderson[5]

[1]University of Michigan
[2]University of Texas at Arlington
[3]University of Michigan-Ann Arbor
[4]Virginia Tech
[5]John Hopkins Univ.

November 30, 2022

Abstract

Ionospheric conductance is a crucial factor in accurately estimating the closure of magnetospheric currents in the ionosphere. Despite its importance in predictive investigations of the magnetosphere - ionosphere coupling, the estimation of ionospheric conductance in the auroral region is precarious in most global first-principles based models. This impreciseness in estimating this auroral conductance impedes both our understanding of the magnetosphere-ionosphere system during extreme space weather events, and predictive capabilities of ground-based magnetic perturbations during extreme driving which generate geomagnetically induced currents. In this article, we address this concern, with the development of an advanced Conductance Model for Extreme Events (CMEE) that estimates the auroral conductance from field aligned current values. CMEE has been developed using nonlinear regression over a year's worth of one-minute resolution output from assimilative maps, specifically including times of extreme driving of the solar wind-magnetosphere-ionosphere system. The model also includes provisions to enhance the conductance in the aurora using additional adjustments to refine the auroral oval. CMEE has been incorporated within the Ridley Ionosphere Model (RIM) of the Space Weather Modeling Framework (SWMF) for usage in space weather simulations. This paper compares performance of CMEE against the existing conductance model in RIM, through a validation process for six space weather events. The performance analysis indicates overall improvement in the ionospheric feedback to the magnetosphere. Specifically, the model is able to improve the prediction of ionospheric currents which impact the simulated and , resulting in substantial improvements in predictive skill.

Conductance Model for Extreme Events : Impact of Auroral Conductance on Space Weather Forecasts

Agnit Mukhopadhyay[1], Daniel T. Welling[2], Michael W. Liemohn[1], Aaron J. Ridley[1], Shibaji Chakraborty[3], and Brian J. Anderson[4]

[1]Climate and Space Sciences and Engineering Department, University of Michigan, Ann Arbor, MI, USA
[2]Department of Physics, University of Texas at Arlington, Arlington, TX, USA
[3]Department of Electrical and Computer Engineering, Virginia Polytechnic Institute and State University, Blacksburg, VA, USA
[4]Applied Physics Laboratory, Johns Hopkins University, Baltimore, MD, USA

Key Points:

- An updated auroral conductance module is built for global models using nonlinear regression & empirical adjustments spanning extreme events.
- Expanded dataset raises the ceiling of conductance values, impacting the polar cap potential, dB/dt & ΔB predictions during extreme events.
- Application of expanded model with empirical oval adjustments refines the conductance pattern, and drastically improves dB/dt predictions.

Corresponding author: Agnit Mukhopadhyay, agnitm@umich.edu

Abstract

Ionospheric conductance is a crucial factor in accurately estimating the closure of magnetospheric currents in the ionosphere. Despite its importance in predictive investigations of the magnetosphere - ionosphere coupling, the estimation of ionospheric conductance in the auroral region is precarious in most global first-principles based models. This impreciseness in estimating this auroral conductance impedes both our understanding of the magnetosphere-ionosphere system during extreme space weather events, and predictive capabilities of ground-based magnetic perturbations during extreme driving which generate geomagnetically induced currents. In this article, we address this concern, with the development of an advanced Conductance Model for Extreme Events (CMEE) that estimates the auroral conductance from field aligned current values. CMEE has been developed using nonlinear regression over a year's worth of one-minute resolution output from assimilative maps, specifically including times of extreme driving of the solar wind-magnetosphere-ionosphere system. The model also includes provisions to enhance the conductance in the aurora using additional adjustments to refine the auroral oval. CMEE has been incorporated within the Ridley Ionosphere Model (RIM) of the Space Weather Modeling Framework (SWMF) for usage in space weather simulations. This paper compares performance of CMEE against the existing conductance model in RIM, through a validation process for six space weather events. The performance analysis indicates overall improvement in the ionospheric feedback to the magnetosphere. Specifically, the model is able to improve the prediction of ionospheric currents which impact the simulated dB/dt and ΔB, resulting in substantial improvements in dB/dt predictive skill.

Plain Language Summary

Electric currents generated in the Earth's space environment due to its magnetic interaction with the Sun leads to charged particle deposition and closure of these currents in the terrestrial upper atmosphere, especially in the high latitude auroral region. The enhancement in the electrical charge carrying capacity as a result of this process in the Earth's upper atmosphere, also known as the ionosphere, is challenging to estimate in most numerical simulations attempting to study the interactive dynamic and chemical processes in the near-Earth region. The inability to accurately estimate this quantity leads to underprediction of severe space weather events that can have adverse impacts on man-made technology like electrical power grids, railway and oil pipelines. In this study, we present a novel modeling approach to address this problem, and provide global simulations with a more accurate estimate on the electrical conductivity of the ionosphere. Through this investigation, we show that the accurate measurement of the charge carriers in the ionosphere using the new model causes substantial improvements in the prediction of space weather on the ground, and significantly advances our understanding of global dynamics causing ground-based space weather.

1 Introduction

The interaction of the solar wind and the terrestrial magnetic field produces magnetospheric current systems such as field aligned currents (FACs) which close through the conductive ionosphere, thereby allowing magnetospheric convection to eventuate (e.g. Axford & Hines, 1961; Dungey, 1963; Iijima & Potemra, 1976). For precise investigations of the magnetospheric feedback on the ionosphere and vice versa, an accurate estimate of the ionospheric conductance is critical for realistic global modeling of the magnetosphere, especially during space weather events (e.g. Merkine et al., 2003, Ridley et al., 2004, Merkin, Sharma, et al., 2005; Merkin, Milikh, et al., 2005, Liemohn et al., 2005). Two dominant sources contribute to the ionosphere's enhanced but finite conductivity - solar extreme ultra-violet (EUV) flux on the dayside, and auroral precipitation in the polar region predominantly on the nightside (Schunk & Nagy, 2009; Newell et al., 2009;

Fuller-Rowell & Evans, 1987). Conductance due to solar EUV radiation is relatively well understood through the use of radiative transfer (e.g. Chapman, 1931). The EUV flux is accounted for in most modern modeling tools as a physics-based empirical function of the solar zenith angle (e.g., Brekke & Moen 1993). Auroral electron and ion precipitation, largely driven by magnetospheric processes, further ionizes neutrals and ions in the ionosphere (e.g., Frahm et al., 1997; Ahn et al., 1998), and enhances the electrical conductivity in the high-latitude auroral regions (Robinson et al., 1987). Since auroral precipitation of charged particles is directly related to variations in the intrinsic magnetic field (e.g., Roederer, 1970), auroral conductance is an important quantity to predict when investigating the ionosphere's impact on the magnetosphere, and vice versa, during strong driving when the global magnetic field changes rapidly (e.g., Welling, 2019).

Although several studies have examined the influence of the ionospheric conductance on the global state of the magnetosphere, ionospheric dynamics and their coupled non-linear feedback system (e.g., Raeder et al., 2001; Ridley et al., 2001, 2004; Liemohn et al., 2005; Wiltberger et al., 2001, 2004; Zhang et al., 2015; Connor et al., 2016; Ozturk et al., 2017), few studies have actually explored the contribution of conductance on space weather forecasts, especially during extreme space weather events. This is very difficult to do with data, since measurements of the ionospheric conductance are notoriously inaccurate (Ohtani et al., 2014). Investigations using global models such as Ridley et al. (2004) have indulged in the broad quantification of the conductance due to EUV illumination and auroral precipitation. Studies such as Wiltberger et al. (2001), Zhang et al. (2015), Yu et al. (2016) and Wiltberger et al. (2017) addressed this further by identifying the source and impact of various contributors to the auroral conductance. Additional evaluations by Perlongo et al. (2017) included the effect of auroral precipitation due to the ring current using a kinetic ring current model coupled to an ionosphere-thermosphere model. Modeling efforts by Ahn et al. (1998), Newell et al. (2009), Korth et al. (2014) have estimated ionospheric auroral conductance through empirical relations, using global quantities like solar wind input, ground-based magnetic perturbations and field aligned currents as inputs. Recently, Robinson et al. (2018) developed an empirical model using incoherent scatter radar measurements against AMPERE FAC estimations, which spanned the St. Patrick's Day Storm of 2015, an event studied extensively for ionospheric disturbances (e.g., Le et al., 2016). In spite of its importance, the impact of auroral conductance during extreme events in global simulations has been hard to determine, due to inaccuracies in conductance estimations within global models, leading to possible underprediction of global quantities like cross polar cap potential (e.g., Honkonen et al., 2013; Mukhopadhyay, 2017), field aligned currents (Anderson et al., 2017), storm indices (Liemohn, McCollough, et al., 2018) and transient ground-based magnetic perturbations (Welling et al., 2018).

With rising operational usage of first-principles-based geospace models in space weather prediction, the need for accurate conductance models is even more necessary. Operational forecasts of the near-Earth space environment using first-principles based global numerical frameworks (e.g., Tóth et al., 2005), combining global magnetohydrodynamic (MHD) models (e.g., Powell et al., 1999; Raeder et al., 2001) with suitable inner magnetospheric models (e.g., De Zeeuw et al., 2004) and ionospheric models (e.g., Ridley & Liemohn, 2002; Wiltberger et al., 2004), have been in use for space weather prediction (Liemohn, Ganushkina, et al., 2018) since the end of the GEM Challenge of 2008-09 (Pulkkinen et al., 2011, 2013, Rastaetter et al. 2013). The procedural assessment specifically presented in Pulkkinen et al. (2013) (hereinafter referred to as *Pulkkinen2013*) to investigate predictive skill of global first-principles-based models in predicting ground-based magnetic perturbations dB/dt, initiated the transition of model usage toward operational prediction at the NOAA Space Weather Prediction Center (SWPC). Several investigations, since then, have further reviewed and systematically addressed the results from this effort, and have suggested rectifications to improve predictive skill (e.g., Honkonen et al., 2013; Glocer et al., 2016; Anderson et al., 2017; Mukhopadhyay, 2017; Liemohn, Ganushkina, et

al., 2018; Liemohn, McCollough, et al., 2018; Welling et al., 2018). In particular, the study by Welling et al. (2017) indicated inherent deficiencies in auroral conductance models used in global models that inhibited them from estimating conductance accurately during extreme space weather events. The study concluded that the inability of global models to estimate the ionospheric conductance accurately during extreme events led to underprediction of dB/dt.

A key conclusion in the study by Welling et al. (2017) (hereinafter referred to as *Welling2017*) questions the dataset used in estimating a geospace model's auroral conductance during extreme weather, and hypothesizes that the inclusion of information from a larger dataset, including sufficient coverage of extreme events, may lead to improvements in a model's space weather predictive metrics during extreme events. The study falls short of addressing supplementary effects due to the auroral oval's pattern estimation in aforementioned models, and the acute effect such a pattern may have on predictive skill. In this paper, we describe the development and validation of an updated empirical auroral conductance model, specifically including data that spans several extreme events, which addresses the concerns raised in *Welling2017*. We use this conductance model within the geospace variant of the Space Weather Modeling Framework (SWMF; Tóth et al., 2005, 2012), identical to the version used operationally at the NOAA Space Weather Prediction Center for space weather forecasting, to investigate the effect of this enhanced conductance model on space weather predictions, and compare these results to the already-existing conductance model within the SWMF. We additionally study the effect of adjusting the pattern of the auroral oval using empirical enhancements based on field aligned current strength, to alter the model's space weather predictions. As a result, in this article, we investigate three major science questions:

1. Addressing *Welling2017*: Does expanding the dataset used to create the initial conductance model help improve space weather predictions?
2. How significant is the improvement in the space weather predictions due to the enhanced auroral oval adjustment parameters?
3. Can the combination of the expanded dataset and an auroral oval enhancement cause significant improvement in the global model's space weather prediction?

In order to address the aforementioned questions, a new **C**onductance **M**odel for **E**xtreme **E**vents (CMEE) has been developed. CMEE is based on the SWMF's empirical auroral conductance model, which uses an inverse-exponential relation to estimate the conductance, and employs an empirically-driven auroral oval adjustment to enhance conductance in regions of strong FACs. A key difference in CMEE, however, is in the dataset it was developed from: CMEE uses one whole year of AMIE data to estimate its conductance. Compared to the old model which was derived from the relatively quiet month of January 1997, minute-data from the whole year of 2003 was utilized to develop CMEE. This included some of the most extreme geospace events ever observed (Cid et al., 2015). In addition to an enlarged training dataset, the value of the empirical coefficients in CMEE are deduced using a non-linear fitting algorithm with suitable extreme boundary conditions that minimizes the absolute error and maximizes the prediction efficiency. The global model configurations used and the science questions addressed in this study, and the subsequent results from this study are described in Sections 2 and 3 respectively, while the algorithm used to develop the advance conductance model and the auroral oval adjustment module have been described in Section 2.2.

2 Methodology

2.1 Simulation Setup

The SWMF is a flexible framework that executes, synchronizes and couples many otherwise independent models together as one. It has performed favorably in predictive

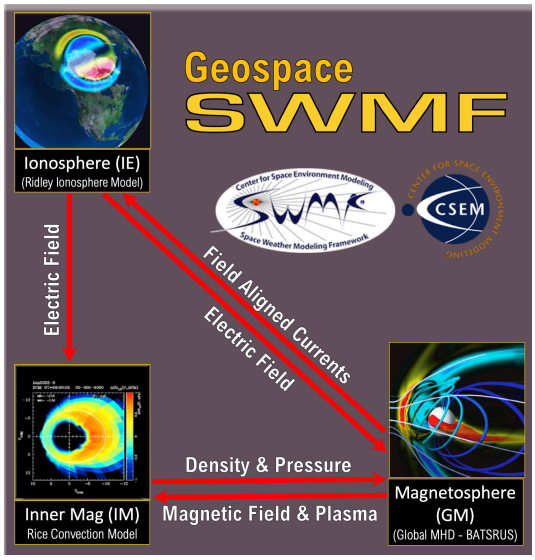

Figure 1. Component layout of the geospace version of the SWMF, same as the layout in *Pulkkinen2013*, used in this study to investigate the role of auroral conductance in space weather prediction.

metric challenges and investigations (e.g., *Pulkkinen2013*; Honkonen et al., 2013; Mukhopadhyay, 2017; Welling et al., 2017; Liemohn, McCollough, et al., 2018), contains an easily-modifiable empirical conductance model in the ionospheric electrodynamics module (Ridley et al., 2004), and is capable of calculating perturbations to the magnetic field (ΔB) by applying Biot-Savart integrals across its domain to estimate magnetometer values virtually (Yu et al., 2010). For this study, we have used the SWMF with three physical modules activated (Figure 1; details below). Identical to the study conducted by *Pulkkinen2013*, the SWMF's geospace version was configured to use three components: Global Magnetosphere (GM), Inner Magnetosphere (IM), and Ionospheric Electrodynamics (IE).

The GM module uses the Block Adaptive Tree Solar-Wind Roe Upwind Scheme (BATS-R-US, Powell et al., 1999; Gombosi et al., 2003) model which solves for the ideal non-relativistic magnetohydrodynamic (MHD) equations in the magnetosphere with an inner boundary at ~ 2.5 Earth radii (R_E).The computational domain for geospace simulations of BATS-R-US extends from $32R_E$ upstream to $224R_E$ downstream in the x direction and $128R_E$ in the y and z coordinates (GSM). The key feature of BATS-R-US is its flexible, block-adaptive Cartesian grid that reserves the highest resolution to regions of interest, ensuring the best combination of performance and accuracy.

The IM region is characterized by closed magnetic field lines and particles of keV energies. This module uses Rice Convection Model (RCM; Wolf et al., 1982). RCM solves for the bounce averaged and isotropic but energy resolved particle distribution of electrons and various ions. RCM receives flux tube volumes from BATS-R-US and returns the pressure and density values to correct those calculated within GM (De Zeeuw et al., 2004). It receives the ionospheric electric potential from the 2-dimensional IE module. The density and temperature initial and boundary values are computed from the GM solution.

The IE component calculates height integrated ionospheric quantities at an altitude of about 110 km. To do so, it receives field aligned currents (FACs) from GM and uses the Ridley Ionosphere Model (RIM, Ridley et al. 2001; Ridley & Liemohn 2002; Ri-

dley et al. 2004), a finite-difference Poisson solver, to calculate the electric potential and horizontal currents using a *prescribed* but dynamic conductance pattern. The module maps FACs at 3.5 Earth radii (R_E) over a two dimensional ionospheric domain, solves for the resulting potential using Ohm's Law (Goodman, 1995), and returns this value to GM and IM. The functioning of and developments to the ionospheric conductance model of RIM are the key features of this article, and are discussed in detail in Section 2.2, along with the development of a more advanced empirical conductance model, CMEE, as a replacement to the aforementioned model.

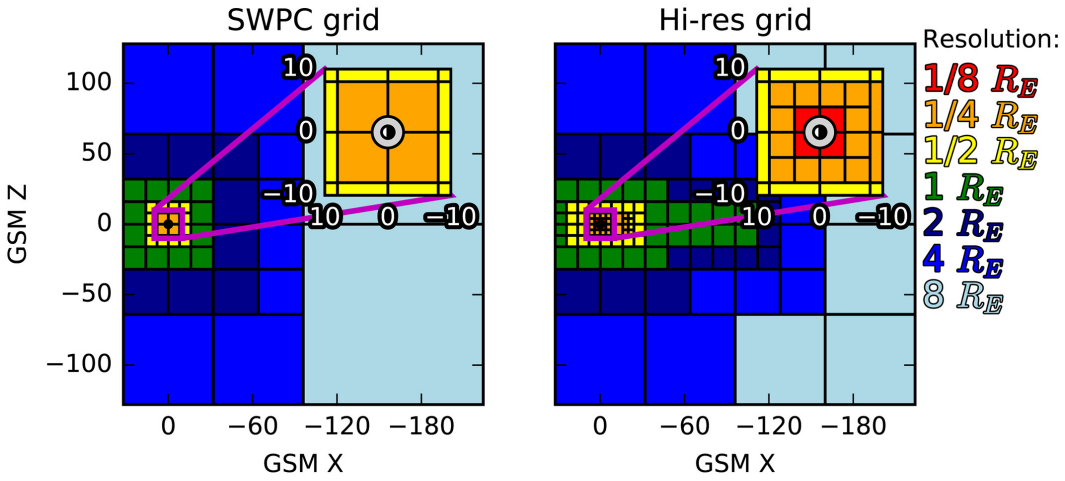

Figure 2. X-Z cuts showing cell sizes in the two MHD grids (reproduced from Haiducek et al., 2017). (Left) The grid used for the *SWPC* configuration (minimum cell size of 0.25 R_E). (Right) The higher-resolution grid used for the *Hi-Res SWPC* configuration (minimum cell size of 0.125 R_E)

In order to simulate a given event, we drive the model using solar wind velocity, magnetic field, density, and temperature, which are used to specify the upstream boundary condition of BATS-R-US. The only other input parameter is F10.7 flux, which is used by IE in computing the dayside EUV-driven ionospheric conductivity (Moen & Brekke, 1993; Ridley et al., 2004). Simulation parameters have been kept similar to *Pulkkinen2013*, throughout the study; the model input conditions and parameters are not tailored to individual events. For this study, we have simulated the events using two different resolutions of BATS-R-US : *SWPC* and *Hi-Res SWPC* (see Figure 2). The *SWPC* configuration is nearly identical to the *Pulkkinen2013* study, and is used operationally by the Space Weather Prediction Center (SWPC). This grid (Figure 2, left) has cell sizes ranging from 8 R_E in the distant tail to 0.25 R_E at the inner boundary, a 16 R_E diameter cube surrounding the Earth, and contains around 1 million cells. The other configuration, *Hi-Res SWPC*, is similar to the previous configuration but uses a higher-resolution grid (among other modifications), to help resolve field aligned currents at the spatial inner boundary. The cell size of this grid (Figure 2, right) varies from 8 R_E in the tail to 0.125 R_E near the Earth, and contains $\sim$ 1.9 million cells. For a detailed description of the above configurations, please refer to Welling & Ridley (2010) and Haiducek et al. (2017).

2.2 Estimation of Auroral Conductance in SWMF

For Ohm's Law to be solved within IE, knowledge of the ionospheric conductance tensor must be known *a priori* (e.g., Goodman, 1995). Within RIM, the legacy code estimating the ionospheric conductance (Ridley et al., 2004) distinguishes two dominant

sources of ionospheric conductance: solar EUV conductance on the dayside, and the auroral precipitative conductance in the polar regions. Supplementary sources of conductance, like nightside "starlight" conductance, seasonal dependencies and polar rain, are added as either functions of the dominant sources of conductance, solar zenith angle or scalar constants. The solar EUV component to the conductance is dependent on the absorption and ion production function of the atmosphere as a function of the solar zenith angle, and is therefore straightforward to estimate using radiometry; the model described in Moen & Brekke (1993) is used to estimate this component of the conductance in most global models (e.g. Raeder et al., 2001 Wiltberger et al., 2004), including RIM. The conductance due to ion and electron precipitation in the auroral region is harder to predict, as this would require the precise knowledge of the charged particle distribution in the magnetosphere. While a physics-based approach to precipitation has been applied in several global models (e.g. Raeder et al., 2001, Zhang et al., 2015, Yu et al., 2016, Perlongo et al., 2017) using kinetic theory (e.g. Knight, 1973), RIM uses a different and simpler approach to estimate the auroral conductance.

2.2.1 Functioning of the Ridley Legacy Model

The auroral conductance module in RIM (briefly described in Ridley et al., 2004), hereinafter referred to as the Ridley Legacy Model (RLM), uses the magnitude and direction of FACs to empirically determine the auroral conductance. This is similar to existing statistical models constructed using FACs to predict and examine precipitation in the auroral ionosphere (e.g. Ahn et al., 1998, Korth et al., 2014, Carter et al., 2016, Robinson et al., 2018). While the numerical domain of RIM spans the entire ionosphere, the RLM domain is considerably limited, spanning from the magnetic pole to magnetic latitude of 60∘ for all magnetic local times (MLT). The auroral conductance at a given magnetic latitude and MLT is assumed to have the form:

$$\Sigma_{HorP} = A_0 - A_1 e^{-A_2^2 |J_{||}|} \tag{1}$$

where Σ_{HorP} denotes the auroral Hall or Pedersen Conductance in the ionosphere (in siemens), $J_{||}$ denotes the field aligned current density (in $\mu A/m^2$), and A_0, A_1 (in siemens) and A_2 (in $m/\mu A^{-1/2}$) are fitting coefficients dependent on location Note that this inverse exponential relation is different from the one mentioned in Ridley et al. (2004); this was a typographical error and the actual relation is given by Equation 1.

The empirical coefficients are the result of fitting based off of conductance and field-aligned current maps derived from assimilative maps of ionospheric electrodynamics (AMIE; Richmond & Kamide, 1988; Kihn & Ridley, 2005) for the month of January 1997 (Boonsiriseth et al., 2001), using ground magnetic perturbations from ∼154 ground-based magnetometers. AMIE derives the auroral conductance using the formulation in Ahn et al. (1998) and Lu et al. (1997), which relate ground-based magnetic perturbations to the Hall and Pedersen conductance, and FACs. The month of runs encompasses $\sim 45,000$ two-dimensional maps of Hall and Pedersen conductance and field-aligned currents. In addition to the empirical maps defining the conductance using FACs, additional auroral oval adjustments were applied to constrain and enhance the conductance in regions of strong FAC driving.

2.2.2 Conductance Adjustments in the Auroral Oval

The conductance pattern in RLM tends to produce broad regions of high conductance that are discontinuous between regions of strong FAC. To improve upon this, an adjustment to the conductance pattern is applied to the estimated pattern described above. The purpose of this is to create a channel for electrojets to form in the model and to improve on the overall electrodynamic result. Though this feature has been implemented in RLM for over a decade, this work is the first to formally describe it and evaluate its impact.

The algorithm for this adjustment starts by estimating the location of the auroral oval. Across all local time values (ϕ) in the model's grid, the geomagnetic co-latitude of the maximum upward FAC at that local time slice ($J_{max}(\phi)$) is obtained. The result is $\theta(\phi)$, or co-latitude as a function of local time. The mean co-latitude, θ_{mean}, weighted by $J_{max}(\phi)$, is then obtained as follows:

$$\theta_{mean} = \frac{\sum \theta(\phi) J_{max}(\phi)}{\sum J_{max}(\phi)} \tag{2}$$

A day-night shift in the center of the oval is calculated using the co-latitudes of $J_{max}(\phi)$ at noon and midnight:

$$\Delta\theta = \frac{J_{noon} * (\theta_{noon} - \theta_{mean}) - J_{midnight} * (\theta_{midnight} - \theta_{mean})}{J_{noon} + J_{midnight}} \tag{3}$$

Using these values, the location of the auroral oval is modeled as follows:

$$\theta(\phi)_{aurora} = \theta_{mean} + \Delta\theta \cos(\phi) \tag{4}$$

With the oval location set, an adjustment is applied to the conductance values about the oval by adjusting the fitting coefficients, A_0 and A_1:

$$A_{0,adj} = A_0 e^{-\frac{d^2}{W^2}} \tag{5}$$

$$A_{1,adj} = A_0 - (A_0 - A_1) e^{-\frac{d^2}{W^2}} \tag{6}$$

...where, for each line of constant local time, d is the co-latitude distance from the oval's locus and W is the width of the oval (default is 2.5°). A baseline conductance about the oval is also applied to avoid nonphysical solutions in regions of low FACs:

$$\Sigma_{baseline} = 1.7(\Sigma_{HorP} + k e^{-\frac{d^2}{W^2}}) \tag{7}$$

where 1.7 is a factor meant to amplify the value of the conductance and k is a constant derived from the aggregate value of the AMIE-derived auroral conductance in regions of high precipitation (magnetic latitude $\in [65°, 80°]$). In this study, the value of k was found to be 7.5 siemens for Hall conductance, and 5 siemens for Pedersen conductance from the AMIE dataset. The net result of this adjustment is that, about the oval, the range of possible conductance values is narrowed and enhanced, and a coherent, sharper auroral conductance pattern arises.

2.2.3 Conductance Model for Extreme Events (CMEE)

Based on the same formulation as RLM, CMEE was developed using a larger dataset in order to include information during intense space weather events ($Dst < -150nT$). For this model, minute-resolution data from AMIE for the whole year of 2003 were utilized to estimate the new fitting coefficients. This significantly increased the model's base dataset from $\sim 45,000$ 2D maps used in RLM, to over $\sim 530,000$ 2D maps used in the present study. In addition to this, the value of the empirical coefficients in CMEE are deduced assuming the same empirical relationship between upward or downward FACs with Hall and Pedersen Conductance, as given by Equation 1. However, unlike RLM which estimates the fitting using equal weighting, the new fitting has been designed using a novel nonlinear regression algorithm which imposes sufficient boundary conditions to ensure that the fitted curve extends to these extreme values and is not just limited to the aggregate value of conductance. This was done by basing the max endpoints of the fittings on the 90% percentile of the FAC values.

Figure 3 (a) presents a representative line plot of Equation 1, and demarcates the conductance vs FAC space into bounded regions designed to estimate fitting coefficients.

The regression algorithm of CMEE classifies FAC data into low and high magnitude bins, separately for upward and downward FACs. The bin boundary for low magnitude FACs, including zero FACs was based on the approximate order of low magnitude FAC density, where asymptotic behavior of conductance values is prevalent and a median value could be found. The median value of the conductance populations in this FAC bin is the minima of the curve $(A_0 - A_1)$. For the low FAC case, setting the bin boundary at $\pm 10^{-4} \mu\mathrm{A/m}^2$ for both upward and downward field aligned currents at all locations led to optimum results. To deduce the conductance maxima as a constant asymptotic value, the FAC dataset was binned into 10 discrete bins with respect to the absolute value of FAC, and the median value of conductance in the bin with the highest FAC values (10th bin) was defined as A_0. A Levenburg-Marquadt (e.g. Pujol, 2007) type bounded least-squares method was used to estimate the non-linear fitting coefficient A_2. The fitting error was defined as the arithmetic mean of the median absolute percentage error (MAPE) and the median symmetric efficiency (ξ) ratio of the data, as defined in Morley et al. (2018). In order to avoid nonphysical solutions from the ionospheric solver due to large gradients (spikiness) in the conductance values, a smoothing filter was applied on the coefficients. The filter was based on a Laplacian mesh smoothing algorithm (e.g. Herrmann, 1976), commonly used in image processing (Yagou et al., 2002) and mesh refinement (Sorkine et al., 2004). The filter is applied such that at each node i,

$$x_i = \begin{cases} x_i & \text{if} \quad \frac{x_i - X}{X} \leq \lambda \\ X & \text{if} \quad \frac{x_i - X}{X} > \lambda \end{cases} \tag{8}$$

where

$$X = \frac{1}{N} \sum_{j=1}^{N} x_j \tag{9}$$

Here, λ is the prescribed difference, N is the number of adjacent vertices to node i, x_j is the position of the j-th adjacent vertex and x_i is the new position for node i. The prescribed difference, similarly defined as the relative difference, is kept at 10%.

Figures 3(b) shows an example of the fitting using the regression algorithm mentioned above over a map of Hall conductance and FAC distribution from AMIE, at the geomagnetic latitude of 62^o and MLT 23 for upward FACs. Figure 3(c) compares the fitting function using CMEE's regression with coefficients from RLM for the same geomagnetic location, but for both upward and downward FACs. The usage of a regression algorithm over a larger span of data shows visible differences in Figure 3(c), where CMEE, denoted in red, is able to push the max value of the conductance to better estimate the quantity during extreme driving. In addition, because of the usage of low FAC bins, the model is also able to provide uniformity in conductance values when field aligned currents are low and/or switch directions. This was previously not included in RLM, denoted in blue in Figure 3(c), as the coefficient values were estimated using uniform weighting on a case-by-case basis separately for upward and downward FACs.

2.3 Event Selection & Prediction Assessment

In order to evaluate CMEE's predictive capabilities and address the science questions mentioned in Section 1, we have simulated a range of space weather events listed in Table 1(a) using variations of the auroral conductance model within the SWMF for comparisons against observations. Since it is a de-facto standard in the space weather community, the present investigation chose to simulate the same events listed in Table 1 of the *Pulkkinen2013* study. Simulation of these events was administered for the two resolutions described in Section 2.1, and using four different variations of the conductance model :-

1. Using only the empirical coefficients of RLM to specify the aurora,
2. Using only the empirical coefficients of CMEE to specify the aurora,

3. Adjusting RLM estimates with the additional enhancements in the auroral oval, and
4. Adjusting CMEE estimates with the additional enhancements in the auroral oval.

Table 1(b) lists the 8 sets of simulations resulting from the above combination.

The study uses data from satellite in-situ measurements and ground-based observations for comparisons against model results. Cross polar cap potential (CPCP) from the model variants was compared against values obtained via the AMIE model and observations from the Super Dual Auroral Radar Network (SuperDARN; e.g. Khachikjan et al., 2008). Since AMIE has a tendency to overpredict CPCP (e.g. Gao, 2012), observations from the SuperDARN were also used to provide a range to the CPCP estimates. Integrated field aligned currents derived from observations by the Active Magnetosphere and Planetary Electrodynamics Response Experiment (AMPERE) mission (Anderson et al., 2014; Waters et al., 2020), estimated using the methodology in Anderson et al. (2017), were used to compare modeled values of FACs. In addition, magnetometer observations from the 12 magnetometer stations listed in Table 2 of the *Pulkkinen2013* study were used to evaluate the predicted ground-based magnetic perturbation ΔB and its temporal variant dB/dt.

Using a similar approach as *Pulkkinen2013*, a binary event analysis (e.g. Jolliffe & Stephenson, 2012; Wilks, 2011) was used to construct a set of relevant performance metrics. An event is defined as the absolute value of a parameter-in-question (any physical quantity like dB/dt) exceeding a predetermined event threshold at any time within a comparison window t_f. For each such window, four outcomes are possible: "Hit" or True Positive (TP; event is observed, and also predicted), "False Alarm" or False Positive (FP; event is not observed, but predicted by model), "Miss" or False Negative (FN; event is observed, but not predicted), and "Correct No Events" or True Negative (TN; event is not observed, and not predicted). Similar to *Pulkkinen2013*, the analysis forecast window t_f was selected to be 20 minutes. The combined results from all events listed in Table 1(a) for a given simulation set are divided into discrete events by the forecast window, creating a contingency table accounting for TPs, FPs, FNs and TNs for a specific threshold. Unlike the *Pulkkinen2013* study, this study chose to discretize the dB/dt into thresholds ranging from 0.1 nT/s to 1.7 nT/s at intervals of 0.1 nT/s, including the thresholds 0.3 nT/s, 0.7 nT/s, 1.1 nT/s and 1.5 nT/s which were used in the former study. In addition to dB/dt, the ΔB values have been discretized using thresholds obtained from Tóth et al. (2014) and *Welling2017*, ranging from 75 to 400 nT at intervals of 25 nT were used.

Once the contingency tables were prepared for each simulation variation, a combination of performance metrics were applied to study improvements. The metrics used in this study and their respective definitions are listed in Table 2. Amongst these metrics, the top four are accuracy measures that help describe the improvement of individual outcomes in a contingency table, while the bottom four metrics quantify the accuracy of a prediction. The Probability of Detection (POD), also called the Positive Prediction Value, is the ratio of positive and negative results, and ranges from 0 to 1, with 1 being a perfect score. The Probability of False Detection (POFD) is the ratio of misses against total negative results. POFD ranges from 0 to 1, with 0 being a perfect score. Along with the POD, these two ratios are accuracy measures of model discrimination. The False Alarm Ratio (FAR), also called False Positive Rate is the ratio between the number of negative events wrongly categorized as positive and the total number of actual negative events (false negatives + true negatives). The Miss Ratio (MR) is defined as the ratio between the number of misses and the sum of hits & misses, describing the conditional probability of a negative test result given that the condition being looked for is present. Both FAR and MR range from 0 to 1, with 0 being a perfect score. These two metrics are a measure of model reliability. The Threat Score (TS), also known as Crit-

(a) List of Events

Event #	Date and Time
1	29 October 2003 06:00 UT - 30 October 06:00 UT
2	14 December 2006 12:00 UT - 16 December 00:00 UT
3	31 August 2001 00:00 UT - 1 September 00:00 UT
4	31 August 2005 10:00 UT - 1 September 12:00 UT
5	5 April 2010 00:00 UT - 6 April 00:00 UT
6	5 August 2011 09:00 UT - 6 August 09:00 UT

(b) List of SWMF Simulations

	RLM Coeffs	*CMEE Coeffs*	*RLM w OA*	*CMEE w OA*
SWPC	Set A	Set B	Set C	Set D
Hi-Res SWPC	Set E	Set F	Set G	Set H

RLM Coeffs - Empirical Coefficients of the Ridley Legacy Model
CMEE Coeffs - Empirical Coefficients of the Conductance Model for Extreme Events
RLM w OA - Ridley Legacy Model, with Auroral Oval Adjustments
CMEE w OA - Conductance Model for Extreme Events, with Auroral Oval Adjustments

Table 1. (a) List of space weather events used in this study to test and validate the different conductance models. This is the same set of events used in *Pulkkinen2013*. (b) A tabular description of all the simulations conducted for this study, binned by SWMF domain variations used: Each set of runs (denoted as 'SET ×', where × is the alphabetic value designated) is a simulation of all space weather events listed in (a), using a particular variation of the auroral conductance model (columns) within a given configuration of the SWMF (rows).

ical Success Index is the ratio of all true positives against the sum of total number of occurrences and false alarms. Due to its neglect of non-occurrences, this score is well suited for scoring predictions of rare events like extreme driving during space weather events. The F_1 score, another measure of a test's accuracy, is defined as the harmonic mean of the POD and the hit rate, given by $(1-MR)$. Similar to the Threat Score, the F_1 score reaches its best value at 1 and worst at 0. The True Skill Score (TSS) or Hanssen-Kuiper Skill Score (Hanssen & Kuipers, 1965) is a performance metric with values ranging from -1 to +1, with 0 representing no skill. The TSS is defined as the difference between the hit rate (given by $1-MR$) and false alarm rate. Lastly, the Heidke Skill Score (HSS; Heidke, 1926) is a performance metric that measures the improvements in a model's results against random chance. Similarly to the TSS, the value of HSS ranges from -1 to +1, with 0 representing no skill. The HSS is popular in space weather forecasting, and has been established as a suitable comparative metric in several space weather studies (Welling & Ridley, 2010, *Pulkkinen2013*, Tóth et al., 2014, Welling et al., 2018).

3 Results & Discussion

3.1 Impact on Global Quantities

Figure 4 exhibits the variations in the pattern and magnitude of Hall conductance for simulations using the low-res *SWPC* configuration. Each dial-plot column displays the high latitude Hall conductance at different time instances from the simulation sets A, B, C and D respectively. The first row shows results from 04:33 UT on October 29, 2003 : toward the beginning of Event 1, before the sudden commencement with the storm

Performance Metric	Acronym	Mathematical Definition
Probability of Detection	POD	$\frac{TP}{(TP+FP)}$
Probability of False Detection	POFD	$\frac{FN}{(FN+TN)}$
False Alarm Ratio	FAR	$\frac{FP}{(FP+TN)}$
Miss Ratio	MR	$\frac{FN}{(TP+FN)}$
Threat Score	TS	$\frac{TP}{(TP+FN+FP)}$
F_1 Score	F_1	$\frac{2TP}{(2TP+FP+FN)}$
True Skill Score	TSS	$\frac{TP}{TP+FN} - \frac{FP}{FP+TN} = (1-MR) - FAR$
Heidke Skill Score	HSS	$\frac{2(TP \times TN - FP \times FN)}{((TP+FP)(FP+TN)+(TP+FN)(FN+TN))}$

Table 2. List of performance metrics used in this study.

index Kp less than 4. The second and third rows, titled Epoch 2 and Epoch 3, compare the four sets at 06:20 UT and 06:46 UT on the same day during the sudden commencement and main phase of Event 1, when $4 \leq Kp < 8$ and $Kp \geq 8$ respectively. As a reference, the bottom line plot shows the Kp throughout the event, along with the predicted Kp from the four simulation variants with the background coloured by the magnitude of Kp - green for $Kp < 4$, yellow for $4 \leq Kp < 8$, and red for $Kp \geq 8$.

Comparing results of Sets A and B, the increased dataset used in CMEE increases the max value of conductance and is capable of capturing auroral dynamics across different activity for every epoch. The addition of oval adjustments visibly alters the pattern of conductance - comparison of Sets A and B with their respective counterparts in Sets C & D illustrate how the adjustments intensify the conductance in regions of high field aligned currents, mimicking discrete arcs. The difference in Sets C & D, while not so apparent in Epochs 1 and 2, are substantially distinct in Epoch 3, when $Kp \geq 8$. In this case, the difference in the conductance caused by the combined usage of the increased dataset spanning extreme events and the additional oval-region enhancement results in a higher conductance peak in Set D. For higher Kp, CMEE increases nightside conductance and lowers dayside conductance. This is because CMEE coefficients, a byproduct of an increased dataset spanning seasonal changes in addition to being estimated using a nonlinear regression algorithm, computes lower dayside conductance and higher nightside conductance in comparison to the RLM coefficients. An unusual feature of using FAC-directed empirical models is the emergence of islands of conductance during the peak of the storm (Epoch 3). These discontinuities are reduced by the inital usage of the smoothing function on the coefficients, and addition of a baseline value in the auroral oval region.

Figure 5 compares integrated field aligned currents (iFACs) observations during Event 5 by AMPERE, against estimates from SWMF. Events 5 and 6 were observed by AMPERE, and compared to models in Anderson et al. (2017). The iFACs were estimated similarly to Anderson et al. (2017) and were used to compare the effect of dataset expansion in the top panel (a), the impact of oval adjustments in the middle panel (b), and the combined influence both in the bottom panel (c). In each of these panels, we compare the low resolution *SWPC* configuration of the SWMF simulations (Sets A, B, C and D) with the *Hi-Res SWPC* configuration simulations (Sets E, F, G and H) to visualize the impact of conductance on the input conditions to IE. While minor variations are caused by the usage of different conductance models, no significant changes are observed either by using the CMEE coefficients or by adjusting the auroral oval. Instead, the results show the *Hi-Res SWPC* simulations being able to better capture the magnitude and dynamics of the iFACs than the *SWPC* configurations. While there are definite changes in the FACs and iFAC values due to the different auroral models, the in-

creased resolution helps to capture more of the FACs, dramatically improving the data-model comparison.

Figure 6 compares simulated cross polar cap potential (CPCP) for all simulation sets against values obtained from AMIE and SuperDARN, for Event 3, which was the only event in this study for which high quality AMIE and SuperDARN data were available. Figure 6 is divided into three groups: in each group, the low res and high res simulations are compared in separate subplots with the topmost group in part (a) illustrating the impact of updated conductance coefficients on CPCP, middle group in part (b) investigating the impact of oval adjustments, and the bottom group in part (c) comparing the combined influence of dataset expansion and oval adjustments The difference between the AMIE CPCP, denoted by the solid black line, and SuperDARN CPCP, denoted by the dot-dashed line, has been demarcated using a thick dark grey region in each subplot to give an envelope of expected values based on the observations-based estimates.

As shown in Figures 4 and 5, the introduction of CMEE and oval adjustments increases the value of the auroral conductance but does not dramatically impact the strength of FACs, for a given domain resolution. Since the electrostatic potential is the direct output of Ohm's Law, an increment in conductance with no substantial change in FACs leads to a lower value of CPCP. This is explicitly observed in part (a), where RLM-driven simulations overestimates the CPCP in both the *SWPC* and *Hi-Res SWPC* cases, in comparison to CMEE-driven simulations. The *Hi-Res* RLM case, denoted in yellow (Frame 6a-ii), particularly stands out because the FAC-driven conductance reaches the ceiling set by the coefficient A_0, i.e. as the magnitude of FACs increases, the value of conductance attains the asymptotic maximum value (A_0) in the given model. Since the median A_0 value is higher in CMEE it is able to give a reasonable CPCP estimate, while RLM's reduced conductance peaks during the strongest driving resulting in the CPCP being an order of magnitude greater. In part (b), conductance increments driven by oval adjustments largely reduces the CPCP, except during the main phase of the event when $Kp > 4$. This is because, during peak driving, the conductance from both models is so large that the oval adjustments do not affect results substantially. In part (c), CMEE-driven CPCP is lower than RLM-driven CPCP, as is expected. The CPCP values from Set D (Frame 6c-i) are too low, indicating that the model is overestimating the conductance which resulted in a lower CPCP. For the *Hi-Res* case in Frame 6c-ii, the higher conductance estimation coupled with better resolved FACs acts in favour of CMEE-driven simulations in Set H, and leads to a more realistic CPCP as shown by the comparison against AMIE and SuperDARN. In all events, simulations driven with RLM tend to have a higher CPCP compared to CMEE, as the conductance ceiling is higher in CMEE than RLM.

Figure 7 illustrates the impact of conductance on dB/dt predictions during Event 2, at two magnetometer stations - the high-latitude magnetometer station at Yellowknife (YKC) located at magnetic latitude (MLat) 68.93° N and magnetic longitude (MLon) 299.36°, and the mid-latitude magnetometer station at Newport (NEW) located at MLat 54.85° N and MLon 304.68°. While YKC and NEW are far apart latitudinally, longitudinally they are separated by less than 5°, making them a good candidate to study the expansion of the auroral oval under strong driving conditions. The background in each subplot, in addition to being coloured by Kp similar to Figures 5 and 6, are darkened to indicate times when the magnetometer was on the nightside. Additionally, dash-dot lines in all subplots indicate the four thresholds chosen in the *Pulkkinen2013* study.

Between 14:08 UT and 18:17 UT on December 14, 2006, as activity increases, massive dB/dt spikes were observed at YKC with values crossing the four *Pulkkinen2013* thresholds. These spikes died down as activity increased, indicated by the increment in the Kp values. From ∼18:20 UT to 07:04 UT on December 15, except for one massive spike at 04:28 UT, dB/dt spikes at YKC barely cross the second and third threshold. During this time period, the magnetometer was mostly on the nightside. Interestingly, all substantial perturbations observed at NEW occur during this same time interval, between 22:21

UT and 07:54 UT. This is an indication that the auroral oval expanded equatorward during this given time interval, with the storm intensifying. This expansion of the oval resulted in latitudinally-high YKC no longer being in the auroral zone and instead being in the polar cap region, while the lower boundaries of the auroral oval reached latitudinally-lower NEW. Starting at 07:54 UT, spikes at NEW died down and were almost negligible throughout the rest of the event. Around the same time, massive spikes crossing all four thresholds were observed again at YKC as the magnetometer station approaches the midnight-dawn sector. The spikes at YKC were observed until 16:33 UT as the magnetometer station rotated to the dawn-noon sector, through the recovery period of the event.

In parts (b) and (c) of Figure 7, modeled dB/dt at YKC and NEW are compared against observations. The topmost panel in part (b) compares modeled dB/dt from Sets E and F addressing the impact of dataset expansion. The middle panel in (b) compares Sets F and H to address the effect of auroral oval adjustments, while the bottom panel compares Sets G and H to study the combined influence of both the expanded dataset and the oval adjustments. In part (c), modeled dB/dt from Sets G and H are compared against observations at NEW. To simplify visualization, the minute-resolution data from both observed and modeled dB/dt values in parts (b) and (c) have been max-filtered for every 10 minute interval. Additionally, the subplot background and threshold lines in parts (b) and (c) are plotted and coloured similarly to part (a).

In the top panel of part (b), the magnitude of the CMEE-simulated dB/dt spikes are mostly at par with or moderately larger than the RLM-simulated spikes through most of the event. Both Sets E and F reasonably modeled the dB/dt during the time interval when the oval expanded and YKC was in the polar cap. However, they were unable to reproduce the heavy spikes that appeared both before and after the time interval, barely crossing the fourth threshold of 1.5 nT/s at any given instance. In the middle panel, both the frequency and magnitude of the dB/dt spikes increased significantly with the introduction of the oval adjustments. While this led to minor improvements in reproducing observations at time intervals when YKC observed heavy spikes, a substantial change occured during the oval expansion when there were minimal dB/dt perturbations in both the observations and the coefficient-driven simulation results but intense spikes at high frequencies in the oval-adjusted simulation output. This increment in dB/dt spikes is dominant in the bottom panel of part (b) in both CMEE and RLM driven simulations. The impact of the dataset expansion combined with the oval adjustment in Set H simulations led to a sharp increase in the magnitude of the spikes, in addition to the sharp rise in frequency. Part (c) indicate that the model does not reproduce the dB/dt spikes at NEW, regardless of the conductance model used. This is in direct contrast to the results from the last panel of part (b) which compares the same model variants but shows multiple intense dB/dt spikes at YKC during the same time interval. This indicates that while usage of CMEE + oval adjustments improved the performance, there were still outstanding issues concerning the expansion and location of the oval that may require a more comprehensive, physics-based approach.

Figure 8 illustrates comparison magnetic perturbations ΔB at the same magnetometer stations during the same event to provide further clarity on the issue of auroral expansion. Part (a) compares the modeled and simulated ΔB at YKC and NEW during the event. At YKC, heavy fluctuations were observed in the ΔB values corresponding with the same time intervals when the massive spikes in dB/dt were observed in Figure 7(a): between 14:21 UT and 18:19 UT, on December 14, and 06:42 UT and 17:07 UT on December 15. The magnitude of ΔB were ≥ 500 nT during these time intervals. At NEW, while all variations in ΔB were comparatively lower (≤ 400 nT), heavy fluctuations were seen during the same time interval when the auroral oval expands and significant dB/dt perturbations in Figure 7(a) occur, between 23:37 UT and 12:07 UT. During the oval expansion phase, YKC-observed ΔB increases steadily with time produc-

ing minimal fluctuations during this period, retroactively indicating why the dB/dt is low.

In parts (b) and (c) of Figure 8, the simulated ΔB from Sets G and H reasonably reproduce the observed ΔB pattern. During the oval expansion phase of the event, the simulated ΔB of both sets fluctuate with higher frequency and magnitude than is observed at YKC, thereby explaining the massive spikes in the simulated dB/dt seen during the same time interval in Figure 7(b). Quantitatively, the Set H simulations exhibit the best performance with a symmetric signed bias percentage (SSPB; Morley et al., 2018) of $\sim 5.6\%$. Here, SSPB measures the symmetric bias in the forecast against the observed values. At NEW, comparison of the simulated ΔB from either sets do not differ substantially with each other, with a negligible difference of $\leq 1\%$ in their respective SSPB. Neither models are able to predict the perturbations during the main phase of the storm between 00:00 UT to 09:00 UT, explaining similarly poor performance in predicting the dB/dt values for this magnetometer. Part (d) compares the individual contributions of the global current systems - auroral Hall and Pedersen currents, field-aligned currents and magnetospheric currents, in the ΔB estimation at YKC and NEW from the Set H simulation. At YKC, auroral and field-aligned currents are the dominant current systems driving perturbations in the magnetic field while magnetospheric currents contribute negligibly. The opposite is true at NEW, where the ΔB variations are mostly driven by changes in the magnetospheric currents and field aligned currents, with auroral currents barely affecting the simulated ΔB even during the peak driving of the system, indicating minimal contribution.

The comparisons in Figures 7 and 8 indicate that in the modeled ΔB and dB/dt values, the auroral currents have little or no impact on mid and low latitude magnetometer predictions as the auroral oval is not able to extend equatorward to these latitudes. While this is expected during quiet conditions, the impact of auroral currents during extreme events can change dynamically with the expansion of the auroral oval, and can extend to much lower latitudes as evidenced by NEW during this event. The impact of this shortcoming on predictive skill has been described in further detail in Section 4.

3.2 Performance Quantification of dB/dt Comparisons

The results from the binary event analysis performed on the dB/dt predictions show that changing the auroral conductance in the global model, either by expanding the dataset or by applying the oval adjustments, led to minimal or no improvement in skill score for the lowest dB/dt threshold, but improved skill for the remaining dB/dt thresholds, with the most improvement in the highest thresholds. Table 3 presents a re-analysis of the results from *Pulkkinen2013*, emphasizing the changes in the HSS of dB/dt results, that were caused by CMEE and the auroral oval adjustments. In part (a) of the table, the expansion of dataset results in the improvement of HSS in each threshold for both the low and high resolution cases, as evidenced by the difference column. This addresses *Welling2017*'s original question, that expansion of the dataset can lead to improvement in dB/dt predictions. In part (b), the HSS improvement caused by oval adjustments to the aurora is more substantial than in part (a), with HSS going up by ~ 0.1 in the highest thresholds for both *SWPC* and *Hi-Res SWPC* configurations. The comparison of both RLM and CMEE combined with oval adjustments in case (c) show similar improvements in predictive skill for the higher dB/dt thresholds when using CMEE with oval adjustments.

Figures 9(a) and (b) provide a quantitative picture of HSS improvement in the dB/dt predictions over many more thresholds. In both subplots, the y-axis is HSS, while the increasing dB/dt thresholds on the x-axis provide a quantitative value of space weather activity. As expected, the HSS scores for all models decreased with increasing threshold value. However, in the most-extreme thresholds CMEE-driven simulations out-peform RLM-driven simulations, with improvements in the HSS of the same order as previously

evidenced in Table 3. The HSS values in the highest dB/dt thresholds for the low-resolution runs of CMEE, in both parts (a) and (b), were either at par or larger than the HSS values for not only the low-resolution but also the high-resolution RLM simulations. This is a significant improvement in the skill score due to CMEE, as this provides an alternate physics-based remedy that otherwise could only be solved numerically. Naturally, the HSS values of the high-resolution CMEE-driven simulations were the highest at almost all thresholds. Using this result, we can partially address the science questions posed in Section 1 that the auroral conductance impacts the dB/dt significantly, and that improvements in the magnitude or pattern of the conductance boosts predictive skill scores for strong driving of the system.

To better quantify the variation in model performance, the values of all performance metrics listed in Table 2 were investigated. Table 4 presents these metrics calculated for all model variants at the high dB/dt threshold of 1.5 nT/s. In this table, the results show the *SWPC* configuration in the left and the *Hi-Res SWPC* configuration in the right, with the worst performance by configuration coloured in orange and the best performance coloured in blue. For both the *SWPC* and *Hi-Res SWPC* configurations, the POD and MR improved quite significantly for CMEE and the oval adjustments, indicating that the number of hits and misses increased and decreased, respectively. In addition, all skill score metrics in the latter half of the table, excluding TSS, indicate best performance for CMEE with oval adjustment variant for both resolutions of the model. The TS and F_1 score increased indicating that the number of hits increased. As has been shown in the previous figure and table, the HSS improves as we switch models to introduce oval adjustments and expansion of the dataset. However, the opposite occured when looking at POFD and FAR values were considered: the application of oval adjustments led to sharply increased FAR values in both low and high res configurations. While the hits and true negatives increased significantly and misses decreased, as supported by the POD and MR values, the number of false alarms increased steadily as the conductance coefficients were changed and jumped significantly with the application of the oval adjustments. This indirectly affected the TSS, which is defined as the difference between the hit rate and miss rate, or mathematically as 1 - (FAR + MR). Since the FAR increased, in spite of the decreased MR, TSS values reduced by more than 0.05 as we switched models. Given that this order of change in skill was similar to what was achievable by changing model resolutions, the increment in false alarms is a significant drawback when using oval adjustments. The aforementioned trend was observed in all dB/dt thresholds from 0.7 nT/s and above, indicating that this was not an isolated case. The performance metrics for the other thresholds have been presented in the supp. material.

3.3 Performance Analysis of ΔB Estimation

Unlike the dB/dt performance quantification using binary event analysis, the usage of the same procedure on ΔB values does not help address the science questions posed in Section 1. Figure 10 describes variation in HSS for predicted ΔB from all model variants against observed values. In comparison to the dB/dt predictions, the change in ΔB predictions were not nearly as drastic for better or worse. Note that the y-axis in Figures 10(a) and (b) are not the same as in Figures 9(a) and (b); the HSS range spanned in the case of ΔB is much shorter than in the case of dB/dt. In part (a), the CMEE-driven predictions show deterioration in the HSS values compared to RLM. However, in comparison to the variation in HSS for dB/dt by the expanded dataset, the variation observed is minimal. The decrease in HSS values was similar, but lesser, in the *Hi-Res* Set F results. In part (b), the variation in ΔB HSS values are negligible when oval adjustments were applied, for both model resolutions. In fact, some higher thresholds in part (b) showed no substantial change in the HSS values with the CMEE-driven simulations. When comparing parts (a) and (b) of Figure 10, the HSS values in part (b) are greater than their respective counterpart in part (a) of the figure for thresholds $\geq 200\ nT$. This indicates that while changing coefficients by increasing the dataset caused more varia-

(a) Impact of Dataset Expansion

Threshold	*SWPC* Configuration			*Hi-Res SWPC* Configuration		
	RLM	CMEE	Difference	RLM	CMEE	Difference
0.3 nT/s	0.521	0.554	+0.033	0.624	0.640	+0.016
0.7 nT/s	0.445	0.478	+0.033	0.526	0.559	+0.033
1.1 nT/s	0.353	0.394	+0.040	0.434	0.466	+0.032
1.5 nT/s	0.285	0.312	+0.027	0.330	0.367	+0.037

(b) Effect of Oval Adjustment (OA)

Threshold	*SWPC* Configuration			*Hi-Res SWPC* Configuration		
	CMEE	CMEE$^+$	Difference	CMEE	CMEE$^+$	Difference
0.3 nT/s	0.554	0.637	+0.083	0.640	0.685	+0.046
0.7 nT/s	0.478	0.556	+0.078	0.559	0.619	+0.060
1.1 nT/s	0.394	0.474	+0.080	0.466	0.525	+0.059
1.5 nT/s	0.312	0.397	+0.085	0.367	0.465	+0.098

(c) Influence of Dataset expansion and OA Combination

Threshold	*SWPC* Configuration			*Hi-Res SWPC* Configuration		
	RLM$^+$	CMEE$^+$	Difference	RLM$^+$	CMEE$^+$	Difference
0.3 nT/s	0.637	0.637	±0.000	0.699	0.685	−0.013
0.7 nT/s	0.498	0.556	+0.058	0.598	0.619	+0.022
1.1 nT/s	0.406	0.474	+0.068	0.492	0.525	+0.033
1.5 nT/s	0.318	0.397	+0.079	0.409	0.465	+0.056

RLM - Empirical Coefficients of the Ridley Legacy Model
CMEE - Empirical Coefficients of the Conductance Model for Extreme Events
RLM$^+$ - Ridley Legacy Model, with Auroral Oval Adjustments
CMEE$^+$ - Conductance Model for Extreme Events, with Auroral Oval Adjustments

Table 3. Comparison of Heidke Skill Scores (HSS) for the space weather events listed in Table 1(a) at the prescribed four dB/dt thresholds (leftmost column) from *Pulkkinen2013*. (a) The top-most table compares HSS for the conductance coefficients of RLM and CMEE; no auroral amelioration added to the model; (b) The middle table compares results simulated using the CMEE using only the empirical conductance coefficients, against another version of the model that uses the CMEE coefficients along with the artificial oval adjustments; (c) The bottom-most table compares the two empirical models with the auroral oval adjustments. Here, green signifies improvement, while red signifies deterioration in prediction value.

tion in the HSS values of individual simulation sets, application of oval adjustments improves overall performance regardless of the coefficients used.

For a more quantitative explanation of the ΔB performance, Table 5 presents values of all performance metrics calculated for all model variants at a high ΔB threshold of 400 nT. The table is similarly structured to Table 4 with the worst performance in each configuration coloured orange and the best performance coloured blue. When comparing the coefficient-driven simulations of RLM and CMEE, substantial variations are not observed in almost all skill scores with a maximum difference of ~ 0.02 for any given skill score and resolution. The same is seen with the simulations driven with oval adjustments, which also do not vary substantially. However, a significant jump is observed in the skill scores when comparing the impact of oval adjustments with oval adjusted sim-

ulations performing better than only coefficient-driven simulations. For both low and high res configurations, TS and F_1 skill scores improve when oval adjustments are applied. This is also seen in the accuracy measures like POD and MR whose values improve, with the POD jumping by a value of ∼0.1 indicating that the number of hits are increasing and number of misses decreasing. Similar to the dB/dt metric analysis and in sharp contrast to the aforementioned performance metrics, the POFD and FAR values are best for simulations driven using non-oval adjustment applications. This is similar to the results in Section 3.2, where false alarms increase as we switch conductance models. Similar to Section 3.2, the trend seen in these performance metrics are not an isolated case for this specific threshold, but observed in all thresholds. The performance metrics for the other thresholds have been presented in the supp. material.

The TSS and HSS do not show substantial differences as the conductance is modified, with the maximum difference between skill scores not being more than ~ 0.05. By comparison, the difference between the best and the worst HSS performance for the dB/dt is ~ 0.11. The results also show that the best HSS and TSS for the *Hi-Res* case are simulations driven by RLM coefficients, which is in direct contrast to the low res case where RLM coefficients consistently underperform for both TSS and HSS. This contrast is as a result of using the same time forecast window t_f as the *Pulkkinen2013* on ΔB predictions. The comparison window t_f of 20 minutes, used in both this study and the *Pulkkinen2013* study for dB/dt predictions, is not long enough to observe severe variations in ΔB perturbations. As an example, the predicted ΔB hardly varies over more than two of the pre-determined thresholds, even during strong driving. In comparison, dB/dt varies over multiple thresholds several times within a t_f. This shows that the metrics used in this study are not totally appropriate to study improvements in ΔB predictions. This could simply be done by increasing the comparison time window, or by using different error or bias metrics. As discussed earlier in Section 3.1 estimation of SSPB in Figure 8 for specific magnetometer stations during Event 2 gives a quantitative understanding of the difference.

4 Analysis

The considerable increase in the frequency and magnitude of dB/dt spikes at YKC with the application of the oval adjustments in Figure 7(b) is closely associated to the domain constraints in RIM. As described in Section 2.2.1, while RIM's simulation domain spans the ionosphere pole-to-pole, the empirical auroral conductance module is limited with a spatial domain spanning the poles to MLat 60^o. This means that in its present configuration the auroral conductance module, be it RLM or CMEE, is bounded at MLat 60^o, with conductance values equatorward of this boundary dropping exponentially and the aurora being constrained poleward of the boundary. The impact of this boundary is clearly indicated in Figure 8(d), where auroral currents are the dominant source of ground ΔB in high latitude regions like YKC, but contribute negligibly at mid latitudinal regions like NEW.

Since application of both the dataset expansion and oval adjustments result in increasing the conductance ceiling during strong driving, CMEE allows more magnetospheric currents to close more dynamically throughout the ionosphere at any given time. In addition, the oval adjustments enhance conductance in regions of high upward FACs thereby changing the pattern of the auroral conductance and reducing the conductance as a function of distance from the empirically constructed oval. The combined effect of these modifications would result in the auroral horizontal currents in RIM's domain being estimated with increased accuracy. This, in turn, leads to a more accurate estimation of the ΔB perturbation and subsequently dB/dt , which are both calculated from the Biot-Savart integral of these current systems (e.g. Yu et al., 2010; Welling, 2019). The conductance modifications due to the two elements (dataset expansion and oval adjustment) lead to noisier results in dB/dt, which leads to increased spikes. These spikes, when correct, in-

Metric	*SWPC* Configuration				*Hi-Res SWPC* Configuration			
	RLM	CMEE	RLM$^+$	CMEE$^+$	RLM	CMEE	RLM$^+$	CMEE$^+$
POD	0.2216	0.2490	0.2668	0.3557	0.2791	0.3406	0.4309	0.5554
POFD	0.0169	0.0194	0.0253	0.0319	0.0262	0.0378	0.0566	0.0784
FAR	0.3306	0.3358	0.3810	0.3674	0.3780	0.4182	0.4597	0.4775
MR	0.1089	0.1057	0.1041	0.0932	0.1026	0.0957	0.0852	0.0693
TS	0.1998	0.2211	0.2291	0.2948	0.2386	0.2736	0.3153	0.3684
F1	0.3330	0.3622	0.3728	0.4553	0.3853	0.4297	0.4795	0.5385
TSS	0.5605	0.5585	0.5150	0.5394	0.5194	0.4861	0.4551	0.4532
HSS	0.2855	0.3120	0.3179	0.3973	0.3297	0.3672	0.4094	0.4647

Table 4. Performance metrics table for predicted dB/dt at the 1.5 nT/s threshold. Listed are all performance metrics defined in Table 2 (Leftmost column) measured for SWMF simulations conducted using RLM Coefficients (denoted by '*RLM*'), CMEE Coefficients (denoted by '*CMEE*'), RLM with oval adjustment (denoted by '*RLM*$^+$') and CMEE with oval adjustment (denoted by '*CMEE*$^+$') simulated using both the *SWPC* and *Hi-Res SWPC* configurations. The orange values show the least desirable metric results, while the blue values signify the best results for this threshold.

crease the number of hits and when incorrect, increase the number of false alarms. The emergence of dB/dt spikes in the modeled data during the oval expansion phase in the bottom subplot of Figure 7(b) demarcates why false alarms increase when the oval adjustment factor is used. In addition to the boundary constraints, false alarms are also caused by sudden shifting of the empirically-estimated auroral oval. These shifts are caused as a result of the sensitive dependence of the oval adjustments to changes in FAC patterns. Sharp changes in the FAC occuring over time scales in the same order of the coupling time cadence cause the empirical estimation of the oval to change rapidly. This brisk movement of the placement of the oval adjustment results in the loci movement of dB/dt spikes, causing unexpected hits and/or false alarms. In all, the aforementioned problems place the auroral oval in the wrong spot which lead to dB/dt spikes, perhaps even at the right time, but wrong location hence increasing the false alarms.

While an increment in the number of false alarms is a significant drawback, the advantages of using the improved conductance model in the SWMF far outweigh this issue. Firstly, the expansion of the dataset in CMEE allows for an increased limit cap on the magnitude of the conductance which results in generating a more realistic cross polar cap potential to be fed back as input to the GM and IM modules. This is essential when conducting numerical experiments investigating the magnetosphere-ionosphere coupling. Secondly, the changes in the conductance pattern in CMEE, as a result of the use of nonlinear regression, physically alters the nightside and dayside auroral conductance pattern when compared to RLM. Using global modeling, this numerical experiment has not only been able to address the question of expanded dataset raised by *Welling2017*, but is also able to discern the impact of ionospheric conductance on space weather forecasting. Finally, both the magnitude and pattern of ionospheric conductance proves to be an important quantity in affecting a global model's dB/dt predictive skill. Given that the dB/dt is an important quantity used in the science community and the industry to predict space weather on the ground, accuracy in the ionospheric conductance is important in our global models. Through this work, the authors present an advanced and more accurate auroral conductance model to address this challenge.

Metric	*SWPC* Configuration				*Hi-Res SWPC* Configuration			
	RLM	CMEE	RLM$^+$	CMEE$^+$	RLM	CMEE	RLM$^+$	CMEE$^+$
POD	0.4602	0.4385	0.5123	0.5224	0.5687	0.5485	0.6440	0.6671
POFD	0.0575	0.0523	0.0616	0.0658	0.0865	0.0901	0.1393	0.1429
FAR	0.2587	0.2500	0.2516	0.2602	0.2982	0.3146	0.3768	0.3745
MR	0.1701	0.1749	0.1568	0.1546	0.1445	0.1508	0.1289	0.1220
TS	0.3965	0.3826	0.4370	0.4413	0.4580	0.4382	0.4635	0.4767
F1	0.5679	0.5534	0.6082	0.6124	0.6283	0.6093	0.6335	0.6457
TSS	0.5712	0.5751	0.5916	0.5851	0.5573	0.5346	0.4943	0.5035
HSS	0.4585	0.4456	0.5015	0.5042	0.5135	0.4898	0.4994	0.5132

Table 5. Performance metrics table for predicted ΔB at the 400 nT threshold. Listed are all performance metrics defined in Table 2 (Leftmost column) measured for SWMF simulations conducted using the same variants as in Table 4. The orange values show the least desirable metric results, while the blue values signify the best results for this threshold.

5 Conclusion

In this work, the development of an advanced auroral conductance model, CMEE has been presented. CMEE has been designed using nonlinear regression to span minute-resolution data generated from AMIE for the whole year of 2003 spanning extreme events. It has additional capability to add physics-driven empirical adjustments to improve the auroral conductance to ensure a larger range on conductance values to better predict the conductance for a broad range of activity. In this study, this model has been used in the SWMF to investigate the impact of auroral conductance on space weather prediction. Simulated results were compared against observed global quantities like polar cap potential, field aligned current intensity and ground-based magnetic perturbation. Additionally, a quantitative investigation was conducted using a binary event analysis similar to the *Pulkkinen2013* study and skill scores for dB/dt and ΔB predictions were computed.

The investigation showed that application of the increased dataset coupled with oval adjustments led to substantial changes in almost all space weather quantities. CMEE allows the auroral conductance to have an increased range of values, attaining a higher ceiling during extreme driving as compared to RLM. Since FACs are largely driven by upstream conditions, they were not drastically impacted by changes in the conductance model. However, since the conductance value increased and FACs varied minimally, the CPCP values were lowered with the usage of CMEE and the oval adjustments. Since, auroral horizontal currents directly impact the ground magnetic perturbation ΔB and its temporal variant dB/dt, the driving of both these quantities were appreciably altered by the application of both the expanded dataset and oval adjustments. While usage of the expanded dataset resulted in a general increase of the modeled dB/dt magnitude, oval adjustments increased the frequency of dB/dt spikes. Neither of these properties were able to improve the modeling of the auroral oval expansion. This resulted in the formation of different regimes in the latitudinal contribution to the ΔB and dB/dt distributions, with negligble contribution of auroral currents in low or mid latitude magnetometer stations in the modeled output during extreme driving .

The results of the binary event analysis conducted on the simulation variants indicated that usage of CMEE with oval adjustments yields best performance, with drastic improvements in the HSS metric at higher activity thresholds. In addition, most performance metrics exhibited favourable changes when applying the CMEE coefficeints and/or oval adjustments, indicating an increase in the number of identified hits and true neg-

atives and a decrease in misses. However, the performance metrics also indicated that the number of false alarms increased with the application of the oval adjustment. This was caused predominantly because of the brisk movement of the empirically-estimated oval, and the latitudinal constraint on the auroral conductance which inhibits the oval from expanding beyond MLat 60°, thereby pushing the auroral currents poleward. While this process increases the number of hits, favourably affecting most performance metrics, it also hurts metrics like TSS due to increased number of false alarms. The binary event analysis of ΔB predictions do not yield definitive results, exhibiting minimal impact on skill scores. This is most likely because the time forecast window of 20 minutes, chosen to study dB/dt forecasts in the original *Pulkkinen2013* study, is limited for the ΔB to exhibit significant change in value so as to jump multiple number of thresholds and therefore produce any meaningful changes in the performance metrics. Outstanding shortcomings of the present analysis such as those mentioned above and additional analysis like estimation of bias and error metrics for various thresholds are steps that we are presently pursuing. Because validation is a process, continued data-model comparisons will be performed in future studies.

The issues causing the misidentification of dB/dt spikes requires a physical solution with numerical modifications to allow the aurora to expand to mid or low latitudes during extreme events. While this could be done with data, an easier and more novel solution would be to drive precipitation from the magnetospheric domains. This could be done by coupling physics-based precipitative inputs from GM and IM modules to estimate electron and ion precipitation in the aurora. This is similar to what has been done in studies like Raeder et al. (2001) and Wiltberger et al. (2001). Such an approach allows for a novel approach to isolate and understand the impact of individual sources of auroral conductance. At the same time, the precipitation pattern of the aurora allows observational data from extreme events to feature prominently in perceiving the accuracy of precipitative fluxes at different MLTs and magnetic latitudes. The development of such a model is presently being undertaken by the authors to address the aforementioned issue (Mukhopadhyay et al., 2018, 2019).

In conclusion, the usage of CMEE designed using an increased dataset coupled with the application of oval adjustment parameters lead to substantial changes in our dB/dt predictions. With the crucial impact that the auroral conductance imparts on global quantities, CMEE would serve as a competent replacement to RLM's coefficient map. The usage of the oval adjustments in the SWMF's auroral conductance estimation is unique and compelling in driving future developments of auroral conductance models to acheive accuracy in the conductance pattern, in addition to the magnitude. Additionally, as evidenced by the skill score analysis, the new model leads to significant improvement in predictive skill of our space weather model.

Acknowledgments

Support for this work has been provided by NASA Grants NNX17AB87G, 80NSSC18K1120, and 80NSSC17K0015, and NSF Grant 1663770. We would like to acknowledge high-performance computing support from Pleaides (allocation 1815) provided by NASA's High-End Computing Capability Programme, and Cheyenne (allocation UUSL0016) provided by NCAR's Computational and Information Systems Laboratory, sponsored by the National Science Foundation. Model result data, input files and observation data are available via https://doi.org/10.7302/nwxp-g551. The Space Weather Modeling Framework is maintained by the University of Michigan Center for Space Environment Modeling and can be obtained at http://csem.engin.umich.edu/tools/swmf. AMIE Results used in this study are maintained at the University of Michigan's Virtual Model Repository (VMR; http://vmr.engin.umich.edu/) by AJR.

The authors would like to thank Dr. Meghan Burleigh for reading a draft manuscript. We thank Dr. Shasha Zou, Dr. Robert Robinson, Dr. Steven Morley and Dr. Gabor Toth for sharing their expertise in the course of this study. A.M. would like to thank Dr. Do-

gacan su Ozturk, Dr. Zhenguang Huang, Dr. Natalia Ganjushkina, Ms. Abigail Azari, Mr. Alexander Shane, Mr. Brian Swiger and Mr. Christopher Bert for sharing their expertise during the development of modeling, curve-fitting and validation tools used in this study.

References

Ahn, B.-H., Richmond, A. D., Kamide, Y., Kroehl, H. W., Emery, B. A., de la Beaujardiére, O., & Akasofu, S.-I. (1998, jul). An ionospheric conductance model based on ground magnetic disturbance data. *Journal of Geophysical Research: Space Physics*, *103*(A7), 14769–14780. Retrieved from http://doi.wiley.com/10.1029/97JA03088 doi: 10.1029/97JA03088

Anderson, B. J., Korth, H., Waters, C. L., Green, D. L., Merkin, V. G., Barnes, R. J., & Dyrud, L. P. (2014). Development of large-scale birkeland currents determined from the active magnetosphere and planetary electrodynamics response experiment. *Geophysical Research Letters*, *41*(9), 3017-3025. Retrieved from https://agupubs.onlinelibrary.wiley.com/doi/abs/10.1002/2014GL059941 doi: 10.1002/2014GL059941

Anderson, B. J., Korth, H., Welling, D. T., Merkin, V. G., Wiltberger, M. J., Raeder, J., ... Rastaetter, L. (2017). Comparison of predictive estimates of high-latitude electrodynamics with observations of global-scale birkeland currents. *Space Weather*, *15*(2), 352-373. Retrieved from https://agupubs.onlinelibrary.wiley.com/doi/abs/10.1002/2016SW001529 doi: 10.1002/2016SW001529

Axford, W. I., & Hines, C. O. (1961). A Unifying Theory of High-Latitude Geophysical Phenomena and Geomagnetic Storms. *Canadian Journal of Physics*, *39*(10), 1433–1464. Retrieved from https://doi.org/10.1139/p61-172 doi: 10.1139/p61-172

Boonsiriseth, A., Thorne, R. M., Lu, G., Jordanova, V. K., Thomsen, M. F., Ober, D. M., & Ridley, A. J. (2001, jul). A semiempirical equatorial mapping of AMIE convection electric potentials (MACEP) for the January 10, 1997, magnetic storm. *Journal of Geophysical Research: Space Physics*, *106*(A7), 12903–12917. Retrieved from http://doi.wiley.com/10.1029/1999JA000332 doi: 10.1029/1999JA000332

Brekke, A., & Moen, J. (1993). Observations of high latitude ionospheric conductances. *Journal of Atmospheric and Terrestrial Physics*, *55*(11), 1493–1512. Retrieved from http://www.sciencedirect.com/science/article/pii/002191699390126J doi: https://doi.org/10.1016/0021-9169(93)90126-J

Carter, J. A., Milan, S. E., Coxon, J. C., Walach, M.-T., & Anderson, B. J. (2016). Average field-aligned current configuration parameterized by solar wind conditions. *Journal of Geophysical Research: Space Physics*, *121*(2), 1294–1307. Retrieved from https://agupubs.onlinelibrary.wiley.com/doi/abs/10.1002/2015JA021567 doi: 10.1002/2015JA021567

Chapman, S. (1931, jan). The absorption and dissociative or ionizing effect of monochromatic radiation in an atmosphere on a rotating earth. *Proceedings of the Physical Society*, *43*(1), 26–45. Retrieved from http://stacks.iop.org/0959-5309/43/i=1/a=305?key=crossref.46895a3aef390982dcfb99f7afc88ced doi: 10.1088/0959-5309/43/1/305

Cid, C., Saiz, E., Guerrero, A., Palacios, J., & Cerrato, Y. (2015). A Carrington-like geomagnetic storm observed in the 21st century. *J. Space Weather Space Clim.*, *5*, A16. Retrieved from https://doi.org/10.1051/swsc/2015017 doi: 10.1051/swsc/2015017

Connor, H. K., Zesta, E., Fedrizzi, M., Shi, Y., Raeder, J., Codrescu, M. V., & Fuller-Rowell, T. J. (2016). Modeling the ionosphere-thermosphere response to a geomagnetic storm using physics-based magnetospheric energy input:

OpenGGCM-CTIM results. *Journal of Space Weather and Space Climate*, *6*, A25. Retrieved from http://www.swsc-journal.org/10.1051/swsc/2016019 doi: 10.1051/swsc/2016019

De Zeeuw, D. L., Sazykin, S., Wolf, R. A., Gombosi, T. I., Ridley, A. J., & Tóth, G. (2004). Coupling of a global MHD code and an inner magnetospheric model: Initial results. *Journal of Geophysical Research: Space Physics*, *109*(A12), 1–14. doi: 10.1029/2003JA010366

Dungey, J. W. (1963, jan). Interactions of solar plasma with the geomagnetic field. *Planetary and Space Science*, *10*, 233–237. Retrieved from https://www.sciencedirect.com/science/article/pii/0032063363900205 doi: 10.1016/0032-0633(63)90020-5

Frahm, R. A., Winningham, J. D., Sharber, J. R., Link, R., Crowley, G., Gaines, E. E., ... Potemra, T. A. (1997, dec). The diffuse aurora: A significant source of ionization in the middle atmosphere. *Journal of Geophysical Research: Atmospheres*, *102*(D23), 28203–28214. Retrieved from http://doi.wiley.com/10.1029/97JD02430 doi: 10.1029/97JD02430

Fuller-Rowell, T. J., & Evans, D. S. (1987). Height-integrated pedersen and hall conductivity patterns inferred from the tiros-noaa satellite data. *Journal of Geophysical Research: Space Physics*, *92*(A7), 7606-7618. Retrieved from https://agupubs.onlinelibrary.wiley.com/doi/abs/10.1029/JA092iA07p07606 doi: 10.1029/JA092iA07p07606

Gao, Y. (2012). Comparing the cross polar cap potentials measured by superdarn and amie during saturation intervals. *Journal of Geophysical Research: Space Physics*, *117*(A8). Retrieved from https://agupubs.onlinelibrary.wiley.com/doi/abs/10.1029/2012JA017690 doi: 10.1029/2012JA017690

Glocer, A., Rasttter, L., Kuznetsova, M., Pulkkinen, A., Singer, H. J., Balch, C., ... Wing, S. (2016). Community-wide validation of geospace model local k-index predictions to support model transition to operations. *Space Weather*, *14*(7), 469-480. Retrieved from https://agupubs.onlinelibrary.wiley.com/doi/abs/10.1002/2016SW001387 doi: 10.1002/2016SW001387

Gombosi, T. I., De Zeeuw, D. L., Powell, K. G., Ridley, A. J., Sokolov, I. V., Stout, Q. F., & Tóth, G. (2003). Adaptive mesh refinement for global magnetohydrodynamic simulation. In J. Büchner, M. Scholer, & C. T. Dum (Eds.), *Space plasma simulation* (pp. 247–274). Berlin, Heidelberg: Springer Berlin Heidelberg. Retrieved from https://doi.org/10.1007/3-540-36530-3_12 doi: 10.1007/3-540-36530-3_12

Goodman, M. L. (1995, aug). A three-dimensional, iterative mapping procedure for the implementation of an ionosphere-magnetosphere anisotropic Ohm's law boundary condition in global magnetohydrodynamic simulations. *Annales Geophysicae*, *13*(8), 843–853. Retrieved from https://doi.org/10.1007/s00585-995-0843-z doi: 10.1007/s00585-995-0843-z

Haiducek, J. D., Welling, D. T., Ganushkina, N. Y., Morley, S. K., & Ozturk, D. S. (2017). SWMF Global Magnetosphere Simulations of January 2005: Geomagnetic Indices and Cross-Polar Cap Potential. *Space Weather*, *15*(12), 1567–1587. Retrieved from https://agupubs.onlinelibrary.wiley.com/doi/abs/10.1002/2017SW001695 doi: 10.1002/2017SW001695

Hanssen, A. W., & Kuipers, W. J. A. (1965). On the relationship between the frequency of rain and various meteorological parameters. *Meded. Verh.*, *81*, 2 – 15.

Heidke, P. (1926). Berechnung des Erfolges und der Güte der Windstärkevorhersagen im Sturmwarnungsdienst. *Geografiska Annaler*, *8*, 301–349.

Herrmann, L. R. (1976). Laplacian-Isoparametric Grid Generation Scheme. *Journal of the Engineering Mechanics Division*, *102*(5), 749–907.

Honkonen, I., Rastätter, L., Grocott, A., Pulkkinen, A., Palmroth, M., Raeder,

J., ... Wiltberger, M. (2013, may). On the performance of global magnetohydrodynamic models in the Earth's magnetosphere. *Space Weather*, *11*(5), 313–326. Retrieved from http://doi.wiley.com/10.1002/swe.20055 doi: 10.1002/swe.20055

Iijima, T., & Potemra, T. A. (1976). The amplitude distribution of fieldaligned currents at northern high latitudes observed by Triad. *Journal of Geophysical Research-Space Physics*, *81*(13), 2165–2174. Retrieved from http://onlinelibrary.wiley.com/doi/10.1029/JA081i013p02165/abstract{%}5Cnpapers3://publication/doi/10.1029/JA081i013p02165 doi: 10.1029/JA081i013p02165

Jolliffe, I. T., & Stephenson, D. B. (2012). *Forecast Verification: A Practitioner's Guide in Atmospheric Science*. John Wiley & Sons. Retrieved from https://books.google.com/books?hl=en{&}lr={&}id=DCxsKQeaBH8C{&}pgis=1

Khachikjan, G. Y., Koustov, A. V., & Sofko, G. J. (2008). Dependence of superdarn cross polar cap potential upon the solar wind electric field and magnetopause subsolar distance. *Journal of Geophysical Research: Space Physics*, *113*(A9). Retrieved from https://agupubs.onlinelibrary.wiley.com/doi/abs/10.1029/2008JA013107 doi: 10.1029/2008JA013107

Kihn, E. A., & Ridley, A. J. (2005). A statistical analysis of the assimilative mapping of ionospheric electrodynamics auroral specification. *Journal of Geophysical Research: Space Physics*, *110*(A7). Retrieved from https://agupubs.onlinelibrary.wiley.com/doi/abs/10.1029/2003JA010371 doi: 10.1029/2003JA010371

Knight, S. (1973). Parallel electric fields. *Planetary and Space Science*. doi: 10.1016/0032-0633(73)90093-7

Korth, H., Zhang, Y., Anderson, B. J., Sotirelis, T., & Waters, C. L. (2014). Statistical relationship between large-scale upward field-aligned currents and electron precipitation. *Journal of Geophysical Research: Space Physics*, *119*(8), 6715–6731. Retrieved from https://agupubs.onlinelibrary.wiley.com/doi/abs/10.1002/2014JA019961 doi: 10.1002/2014JA019961

Le, G., Lhr, H., Anderson, B. J., Strangeway, R. J., Russell, C. T., Singer, H., ... Torbert, R. B. (2016). Magnetopause erosion during the 17 march 2015 magnetic storm: Combined field-aligned currents, auroral oval, and magnetopause observations. *Geophysical Research Letters*, *43*(6), 2396-2404. Retrieved from https://agupubs.onlinelibrary.wiley.com/doi/abs/10.1002/2016GL068257 doi: 10.1002/2016GL068257

Liemohn, M. W., Ganushkina, N. Y., De Zeeuw, D. L., Rastaetter, L., Kuznetsova, M., Welling, D. T., ... van der Holst, B. (2018). Real-time swmf at ccmc: Assessing the dst output from continuous operational simulations. *Space Weather*, *16*(10), 1583-1603. Retrieved from https://agupubs.onlinelibrary.wiley.com/doi/abs/10.1029/2018SW001953 doi: 10.1029/2018SW001953

Liemohn, M. W., McCollough, J. P., Jordanova, V. K., Ngwira, C. M., Morley, S. K., Cid, C., ... Vasile, R. (2018). Model evaluation guidelines for geomagnetic index predictions. *Space Weather*, *16*(12), 2079-2102. Retrieved from https://agupubs.onlinelibrary.wiley.com/doi/abs/10.1029/2018SW002067 doi: 10.1029/2018SW002067

Liemohn, M. W., Ridley, A. J., Brandt, P. C., Gallagher, D. L., Kozyra, J. U., Ober, D. M., ... DeMajistre, R. (2005, dec). Parametric analysis of nightside conductance effects on inner magnetospheric dynamics for the 17 April 2002 storm. *Journal of Geophysical Research*, *110*(A12), A12S22. Retrieved from http://doi.wiley.com/10.1029/2005JA011109 doi: 10.1029/2005JA011109

Lu, G., Siscoe, G. L., Richmond, A. D., Pulkkinen, T. I., Tsyganenko, N. A., Singer, H. J., & Emery, B. A. (1997). Mapping of the ionospheric field-aligned currents to the equatorial magnetosphere. *Journal of Geophysical*

Research: Space Physics, *102*(A7), 14467–14476. Retrieved from https://agupubs.onlinelibrary.wiley.com/doi/abs/10.1029/97JA00744 doi: 10.1029/97JA00744

Merkin, V. G., Milikh, G., Papadopoulos, K., Lyon, J., Dimant, Y. S., Sharma, A. S., ... Wiltberger, M. (2005, nov). Effect of anomalous electron heating on the transpolar potential in the LFM global MHD model. *Geophysical Research Letters*, *32*(22), n/a–n/a. Retrieved from http://doi.wiley.com/10.1029/2005GL023315 doi: 10.1029/2005GL023315

Merkin, V. G., Sharma, A. S., Papadopoulos, K., Milikh, G., Lyon, J., & Goodrich, C. (2005, sep). Global MHD simulations of the strongly driven magnetosphere: Modeling of the transpolar potential saturation. *Journal of Geophysical Research: Space Physics*, *110*(A9). Retrieved from http://doi.wiley.com/10.1029/2004JA010993 doi: 10.1029/2004JA010993

Merkine, V. G., Papadopoulos, K., Milikh, G., Sharma, A. S., Shao, X., Lyon, J., & Goodrich, C. (2003, dec). Effects of the solar wind electric field and ionospheric conductance on the cross polar cap potential: Results of global MHD modeling. *Geophysical Research Letters*, *30*(23), n/a–n/a. Retrieved from http://doi.wiley.com/10.1029/2003GL017903 doi: 10.1029/2003GL017903

Moen, J., & Brekke, A. (1993, may). The solar flux influence on quiet time conductances in the auroral ionosphere. *Geophysical Research Letters*, *20*(10), 971–974. Retrieved from http://doi.wiley.com/10.1029/92GL02109 doi: 10.1029/92GL02109

Morley, S. K., Brito, T. V., & Welling, D. T. (2018). Measures of Model Performance Based On the Log Accuracy Ratio. *Space Weather*, *16*(1), 69–88. Retrieved from https://agupubs.onlinelibrary.wiley.com/doi/abs/10.1002/2017SW001669 doi: 10.1002/2017SW001669

Mukhopadhyay, A. (2017). *Statistical Comparison of Magnetopause Distances and CPCP Estimation by Global MHD Models* (Tech. Rep.). Retrieved from https://ccmc.gsfc.nasa.gov/RoR{_}WWW/SWREDI/contest-presentations/2017/Statistical{_}Comparison{_}of{_}MP{_}Distances{_}and{_}CPCP{_}CCMC{_}Contest{_}2{_}AgnitM.pdf doi: https://doi.org/10.1002/essoar.10502157.1

Mukhopadhyay, A., Welling, D., Burleigh, M., Ridley, A., Liemohn, M., Anderson, B., & Gjerloev, J. (2019, dec). Conductance in the Aurora: Influence of Magnetospheric Contributors. In *Agu fall meeting abstracts* (Vol. 2019, pp. SA41B–3169). Retrieved from https://ui.adsabs.harvard.edu/abs/2019AGUFMSA41B3169M/abstract doi: doi.org/10.1002/essoar.10502150.1

Mukhopadhyay, A., Welling, D., Liemohn, M., Zou, S., & Ridley, A. (2018, dec). Challenges in Space Weather Prediction: Estimation of Auroral Conductance. In *Agu fall meeting abstracts* (Vol. 2018, pp. SA33B–3462). Retrieved from https://ui.adsabs.harvard.edu/abs/2018AGUFMSA33B3462M/abstract

Newell, P. T., Sotirelis, T., & Wing, S. (2009, sep). Diffuse, monoenergetic, and broadband aurora: The global precipitation budget. *Journal of Geophysical Research: Space Physics*, *114*(A9). Retrieved from http://doi.wiley.com/10.1029/2009JA014326 doi: 10.1029/2009JA014326

Ohtani, S., Wing, S., Merkin, V. G., & Higuchi, T. (2014, jan). Solar cycle dependence of nightside field-aligned currents: Effects of dayside ionospheric conductivity on the solar wind-magnetosphere-ionosphere coupling. *Journal of Geophysical Research: Space Physics*, *119*(1), 322–334. Retrieved from http://doi.wiley.com/10.1002/2013JA019410 doi: 10.1002/2013JA019410

Ozturk, D. S., Zou, S., & Slavin, J. A. (2017). IMF By effects on ground magnetometer response to increased solar wind dynamic pressure derived from global MHD simulations. *Journal of Geophysical Research: Space Physics*. doi: 10.1002/2017JA023903

Perlongo, N. J., Ridley, A. J., Liemohn, M. W., & Katus, R. M. (2017, apr). The

effect of ring current electron scattering rates on magnetosphere-ionosphere coupling. *Journal of Geophysical Research: Space Physics*, *122*(4), 4168–4189. Retrieved from http://doi.wiley.com/10.1002/2016JA023679 doi: 10.1002/2016JA023679

Powell, K. G., Roe, P. L., Linde, T. J., Gombosi, T. I., & Zeeuw, D. L. D. (1999). A Solution-Adaptive Upwind Scheme for Ideal Magnetohydrodynamics. *Journal of Computational Physics*, *154*(2), 284–309. Retrieved from http://www.sciencedirect.com/science/article/pii/S002199919996299X doi: https://doi.org/10.1006/jcph.1999.6299

Pujol, J. (2007). The solution of nonlinear inverse problems and the Levenberg-Marquardt method. *Geophysics*, *72*(4), W1–W16. Retrieved from https://doi.org/10.1190/1.2732552 doi: 10.1190/1.2732552

Pulkkinen, A., Kuznetsova, M., Ridley, A., Raeder, J., Vapirev, A., Weimer, D., ... Chulaki, A. (2011, feb). Geospace Environment Modeling 2008-2009 Challenge: Ground magnetic field perturbations. *Space Weather*, *9*(2), n/a–n/a. Retrieved from http://doi.wiley.com/10.1029/2010SW000600 doi: 10.1029/2010SW000600

Pulkkinen, A., Rastätter, L., Kuznetsova, M., Singer, H., Balch, C., Weimer, D., ... Weigel, R. (2013, jun). Community-wide validation of geospace model ground magnetic field perturbation predictions to support model transition to operations. *Space Weather*, *11*(6), 369–385. Retrieved from http://doi.wiley.com/10.1002/swe.20056 doi: 10.1002/swe.20056

Raeder, J., McPherron, R. L., Frank, L. A., Kokubun, S., Lu, G., Mukai, T., ... Slavin, J. A. (2001). Global simulation of the Geospace Environment Modeling substorm challenge event. *Journal of Geophysical Research-Space Physics*, *106*(A1), 381–395. doi: 10.1029/2000ja000605

Richmond, A. D., & Kamide, Y. (1988). Mapping electrodynamic features of the high-latitude ionosphere from localized observations - Technique. *Journal of Geophysical Research*, *93*(A6), 5741–5759. doi: 10.1029/JA093iA06p05741

Ridley, A. J., De Zeeuw, D. L., Gombosi, T. I., & Powell, K. G. (2001). Using steady state MHD results to predict the global state of the magnetosphere-ionosphere system. *Journal of Geophysical Research*, *106*(A12), 30067. Retrieved from http://adsabs.harvard.edu/abs/2001JGR...10630067R doi: 10.1029/2000JA002233

Ridley, A. J., Gombosi, T. I., & De Zeeuw, D. L. (2004). Ionospheric control of the magnetosphere: conductance. *Annales Geophysicae*, *22*(2), 567–584. Retrieved from https://hal.archives-ouvertes.fr/hal-00317238/ doi: 10.5194/angeo-22-567-2004

Ridley, A. J., & Liemohn, M. W. (2002, aug). A model-derived storm time asymmetric ring current driven electric field description. *Journal of Geophysical Research: Space Physics*, *107*(A8), SMP 2–1–SMP 2–12. Retrieved from http://doi.wiley.com/10.1029/2001JA000051 doi: 10.1029/2001JA000051

Robinson, R. M., Vondrak, R. R., Miller, K., Dabbs, T., & Hardy, D. (1987, mar). On calculating ionospheric conductances from the flux and energy of precipitating electrons. *Journal of Geophysical Research*, *92*(A3), 2565. Retrieved from http://doi.wiley.com/10.1029/JA092iA03p02565 doi: 10.1029/JA092iA03p02565

Robinson, R. M., Zhang, Y., Anderson, B. J., Zanetti, L. J., Korth, H., & Fitzmaurice, A. (2018). Statistical relations between field-aligned currents and precipitating electron energy flux. *Geophysical Research Letters*, *45*(17), 8738-8745. Retrieved from https://agupubs.onlinelibrary.wiley.com/doi/abs/10.1029/2018GL078718 doi: 10.1029/2018GL078718

Roederer, J. G. (1970). *Dynamics of Geomagnetically Trapped Radiation (Vol. 2)*. Berlin, Heidelberg: Springer Berlin Heidelberg. doi: https://doi.org/10.1007/978-3

-642-49300-3

Schunk, R., & Nagy, A. (2009). *Ionospheres: Physics, Plasma Physics, and Chemistry* (2nd ed.). Cambridge University Press. doi: 10.1017/CBO9780511635342

Sorkine, O., Cohen-Or, D., Lipman, Y., Alexa, M., Rössl, C., & Seidel, H.-P. (2004). Laplacian surface editing. In *Proceedings of the 2004 eurographics/acm siggraph symposium on geometry processing* (p. 175184). New York, NY, USA: Association for Computing Machinery. Retrieved from https://doi.org/10.1145/1057432.1057456 doi: 10.1145/1057432.1057456

Tóth, G., Meng, X., Gombosi, T. I., & Rastätter, L. (2014). Predicting the time derivative of local magnetic perturbations. *Journal of Geophysical Research: Space Physics*, *119*(1), 310–321. Retrieved from https://agupubs.onlinelibrary.wiley.com/doi/abs/10.1002/2013JA019456 doi: 10.1002/2013JA019456

Tóth, G., Sokolov, I. V., Gombosi, T. I., Chesney, D. R., Clauer, C. R., De Zeeuw, D. L., ... Kóta, J. (2005, dec). Space Weather Modeling Framework: A new tool for the space science community. *Journal of Geophysical Research*, *110*(A12), A12226. Retrieved from http://doi.wiley.com/10.1029/2005JA011126 doi: 10.1029/2005JA011126

Tóth, G., van der Holst, B., Sokolov, I. V., De Zeeuw, D. L., Gombosi, T. I., Fang, F., ... Opher, M. (2012). Adaptive numerical algorithms in space weather modeling. *Journal of Computational Physics*, *231*(3), 870–903. doi: 10.1016/j.jcp.2011.02.006

Waters, C. L., Anderson, B. J., Green, D. L., Korth, H., Barnes, R. J., & Vanhamäki, H. (2020). Science data products for ampere. In M. W. Dunlop & H. Lühr (Eds.), *Ionospheric multi-spacecraft analysis tools: Approaches for deriving ionospheric parameters* (pp. 141–165). Cham: Springer International Publishing. Retrieved from https://doi.org/10.1007/978-3-030-26732-2_7 doi: 10.1007/978-3-030-26732-2_7

Welling, D. T. (2019). Magnetohydrodynamic models of b and their use in gic estimates. In *Geomagnetically induced currents from the sun to the power grid* (p. 43-65). American Geophysical Union (AGU). Retrieved from https://agupubs.onlinelibrary.wiley.com/doi/abs/10.1002/9781119434412.ch3 doi: 10.1002/9781119434412.ch3

Welling, D. T., Anderson, B. J., Crowley, G., Pulkkinen, A. A., & Rastätter, L. (2017, jan). Exploring predictive performance: A reanalysis of the geospace model transition challenge. *Space Weather*, *15*(1), 192–203. Retrieved from http://doi.wiley.com/10.1002/2016SW001505 doi: 10.1002/2016SW001505

Welling, D. T., Ngwira, C. M., Opgenoorth, H., Haiducek, J. D., Savani, N. P., Morley, S. K., ... Liemohn, M. (2018). Recommendations for next-generation ground magnetic perturbation validation. *Space Weather*, *16*(12), 1912-1920. Retrieved from https://agupubs.onlinelibrary.wiley.com/doi/abs/10.1029/2018SW002064 doi: 10.1029/2018SW002064

Welling, D. T., & Ridley, A. J. (2010). Exploring sources of magnetospheric plasma using multispecies MHD. *Journal of Geophysical Research: Space Physics*, *115*(A4). Retrieved from https://agupubs.onlinelibrary.wiley.com/doi/abs/10.1029/2009JA014596 doi: 10.1029/2009JA014596

Wilks, D. S. (2011). *Statistical methods in the atmospheric sciences* (3rd ed.). Academic Press.

Wiltberger, M., Merkin, V., Zhang, B., Toffoletto, F., Oppenheim, M., Wang, W., ... Stephens, G. K. (2017, may). Effects of electrojet turbulence on a magnetosphere-ionosphere simulation of a geomagnetic storm. *Journal of Geophysical Research: Space Physics*, *122*(5), 5008–5027. Retrieved from http://doi.wiley.com/10.1002/2016JA023700 doi: 10.1002/2016JA023700

Wiltberger, M., Wang, W., Burns, A. G., Solomon, S. C., Lyon, J. G., & Goodrich, C. C. (2004). Initial results from the coupled magnetosphere ionosphere ther-

mosphere model: magnetospheric and ionospheric responses. *Journal of Atmospheric and Solar-Terrestrial Physics*, *66*(15), 1411–1423. Retrieved from http://www.sciencedirect.com/science/article/pii/S136468260400149X doi: https://doi.org/10.1016/j.jastp.2004.03.026

Wiltberger, M., Weigel, R. S., Lotko, W., & Fedder, J. A. (2001). Modeling seasonal variations of auroral particle precipitation in a global-scale magnetosphere-ionosphere simulation. *Journal of Geophysical Research-Space Physics*, *114*(A1), 381–395. doi: 10.1029/2008JA013108

Wolf, R. A., Harel, M., Spiro, R. W., Voigt, G.-H., Reiff, P. H., & Chen, C.-K. (1982, aug). Computer simulation of inner magnetospheric dynamics for the magnetic storm of July 29, 1977. *Journal of Geophysical Research*, *87*(A8), 5949. Retrieved from http://doi.wiley.com/10.1029/JA087iA08p05949 doi: 10.1029/JA087iA08p05949

Yagou, H., Ohtake, Y., & Belyaev, A. (2002, July). Mesh smoothing via mean and median filtering applied to face normals. In *Geometric modeling and processing. theory and applications. gmp 2002. proceedings* (p. 124-131). doi: 10.1109/GMAP.2002.1027503

Yu, Y., Jordanova, V. K., Ridley, A. J., Albert, J. M., Horne, R. B., & Jeffery, C. A. (2016). A new ionospheric electron precipitation module coupled with ram-scb within the geospace general circulation model. *Journal of Geophysical Research: Space Physics*, *121*(9), 8554-8575. Retrieved from https://agupubs.onlinelibrary.wiley.com/doi/abs/10.1002/2016JA022585 doi: 10.1002/2016JA022585

Yu, Y., Ridley, A. J., Welling, D. T., & Tóth, G. (2010, aug). Including gap region field-aligned currents and magnetospheric currents in the MHD calculation of ground-based magnetic field perturbations. *Journal of Geophysical Research: Space Physics*, *115*(A8). Retrieved from http://doi.wiley.com/10.1029/2009JA014869 doi: 10.1029/2009JA014869

Zhang, B., Lotko, W., Brambles, O., Wiltberger, M., & Lyon, J. (2015). Electron precipitation models in global magnetosphere simulations. *Journal of Geophysical Research: Space Physics*, *120*(2), 1035–1056. Retrieved from https://agupubs.onlinelibrary.wiley.com/doi/abs/10.1002/2014JA020615 doi: 10.1002/2014JA020615

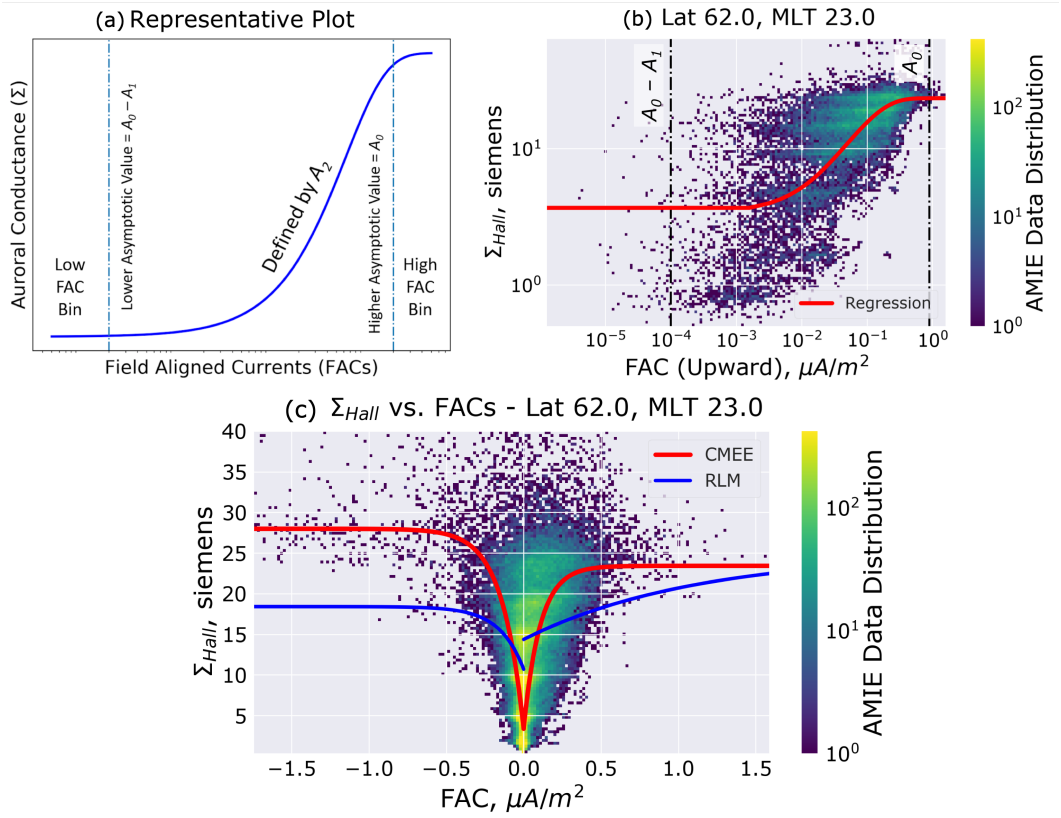

Figure 3. Example Fitting of the Conductance Model for Extreme Events (CMEE) - (a) Representative Line Plot of Auroral Conductance (Hall or Pedersen, in siemens) vs. Field Aligned Currents (FACs, Upward or Downward, in $\mu A/m^2$) through Equation 1 denoting the three regions of interest - low and high FAC bins used to estimate the values of A_0 and A_1, while the region in between these bins defining the curve using regression of A_2. (b) An example log-log plot of the AMIE data showing the scatter of Hall Conductance versus Upward Field Aligned Currents, at magnetic latitude of 68^o and magnetic local time (MLT) 23 in the nightside auroral zone. Alongside the data spread, the regression line is plotted in red with the dot-dashed lines exhibiting the low and high FAC bins. (c) The distribution of AMIE data from 2003 showing the scatter of Hall Conductance versus all Field Aligned Currents plotted along the line plots of RLM and CMEE, denoted in blue and red respectively, at 68^o magnetic latitude and 23 MLT. Note this distribution plot is in linear scale compared to the similar plot part (b), which is in logarithmic scale.

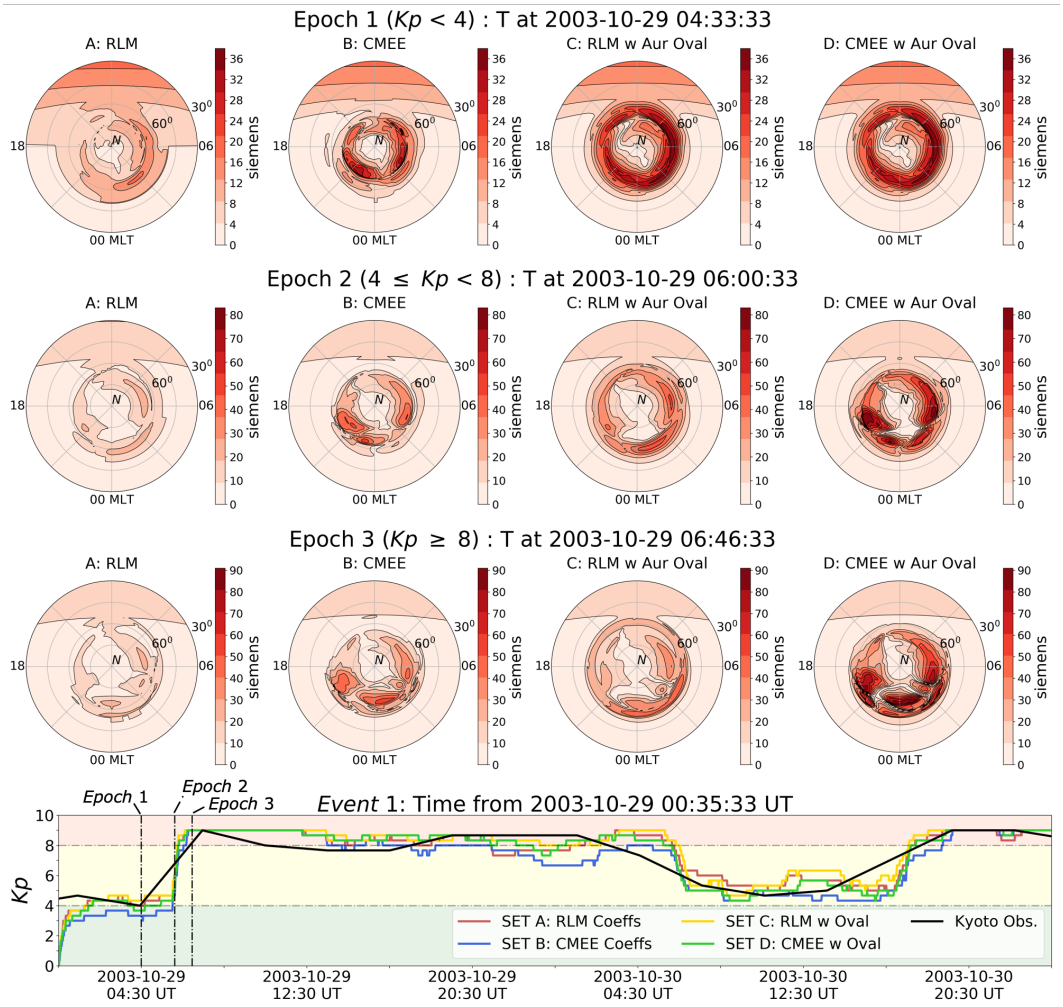

Figure 4. A comparison of Hall conductance values from different conductance model variants. Dial plots from (left to right) simulation sets A, B, C and D at time instances during Event 1 (Epoch 1, Top Row) when $Kp < 4$, (Epoch 2, Second Row) when $4 \leq Kp < 8$, and (Epoch 3, Third Row) when $Kp \geq 8$. (Bottom Subplot) Comparison of Kp from the Kyoto Observatory (in black) against simulated Kp from simulationsets A (in red), B (in blue), C (in gold) and D (in green). Additionally, the plot background is coloured by the Kp, green signifying $Kp < 4$, yellow signifying $4 \leq Kp < 8$, and red signifying $Kp \geq 8$.

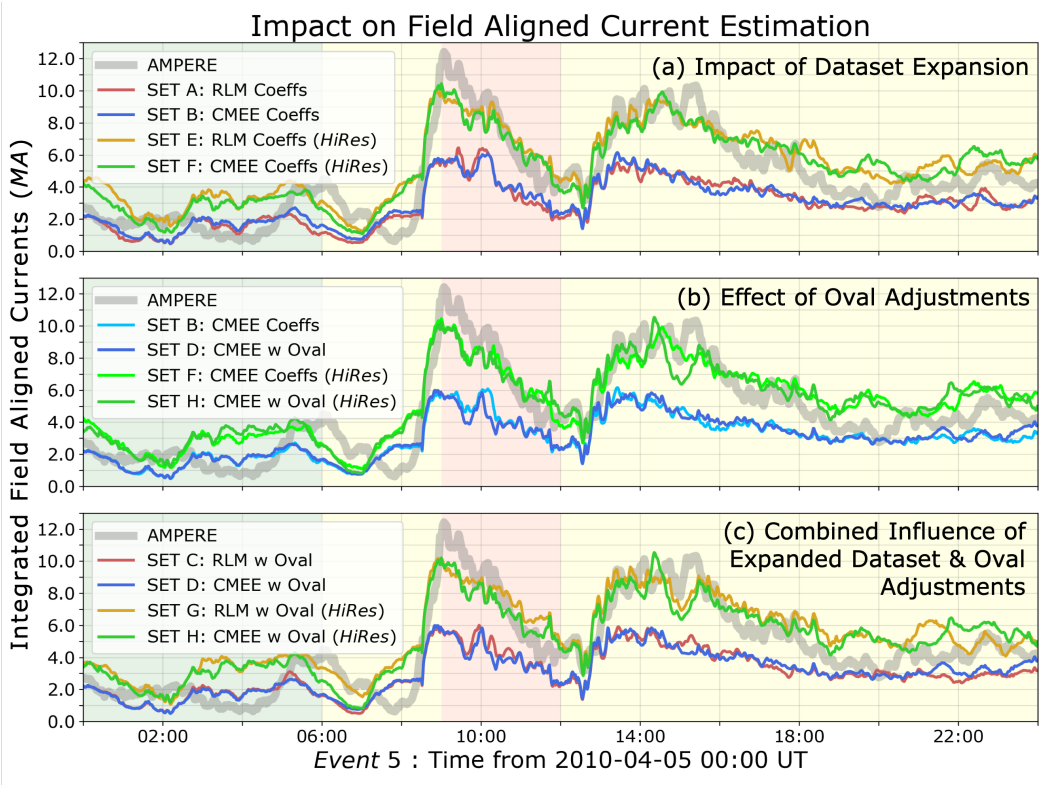

Figure 5. Time series comparison of integrated field aligned currents (iFACs) for Events 5 spanning the storm main phase from AMPERE (gray line) and the eight simulation sets of the SWMF. Goal of each frame: Top Frame (a) illustrates the impact of dataset expansion on iFACs by comparing Sets A (in red), B (in blue), E (in gold) and D (in green). Middle Frame (b) displays the effect of oval adjustments by comparing Sets B (in light blue), D (in blue), F (in light green) and H (in green). Bottom Frame (c) presents the combined influence of dataset expansion and oval adjustments by comparing Sets C (in red), D (in blue), G (in gold) and H (in green). The plot background is coloured by the Kp, green signifying $Kp < 4$, yellow signifying $4 \leq Kp < 8$, and red signifying $Kp \geq 8$.

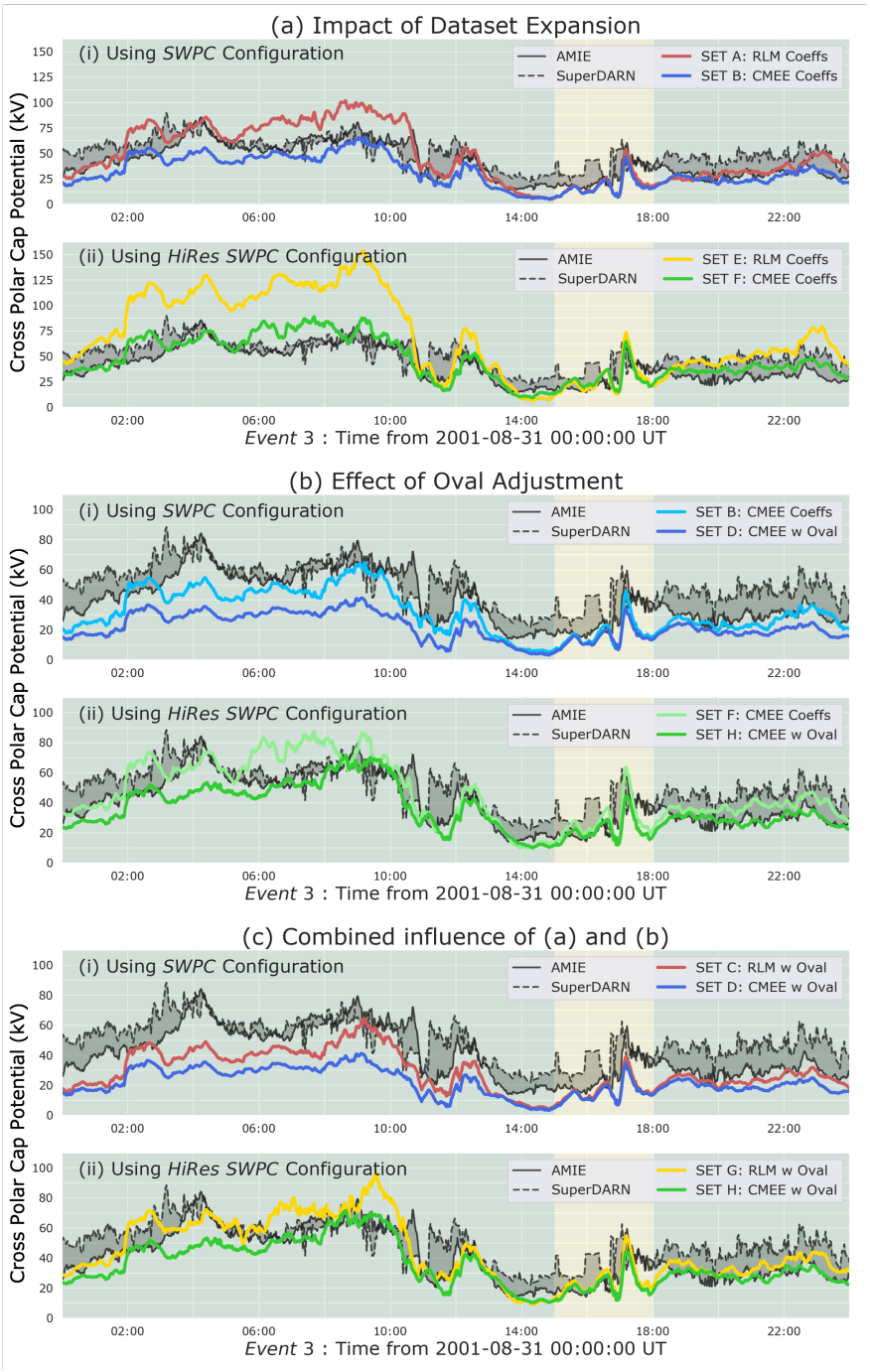

Figure 6. Time series comparison of cross polar cap potential (CPCP) for Event 3 comparing observations from AMIE, SuperDARN, and the eight configurations of the SWMF. Traces show AMIE in solid black, SuperDARN in dashed black, with the difference region between the datasets coloured gray. The SWMF simulations are coloured similarly to Figure 5. Goal of each frame: Top Frame (a) illustrates the impact of dataset expansion on iFACs by comparing (i) Sets A & B in upper panel, and (ii) Sets E & D in bottom panel. Middle Frame (b) displays the effect of oval adjustments by comparing (i) Sets B & D in upper panel, and (ii) F & H (in green) in bottom panel. Bottom Frame (c) presents the combined influence of dataset expansion and oval adjustments by comparing (i) Sets C & D in top panel, and (ii) G & H in bottom panel. The plot background is coloured by the Kp, green signifying $Kp < 4$, and yellow signifying $4 \leq Kp < 8$.

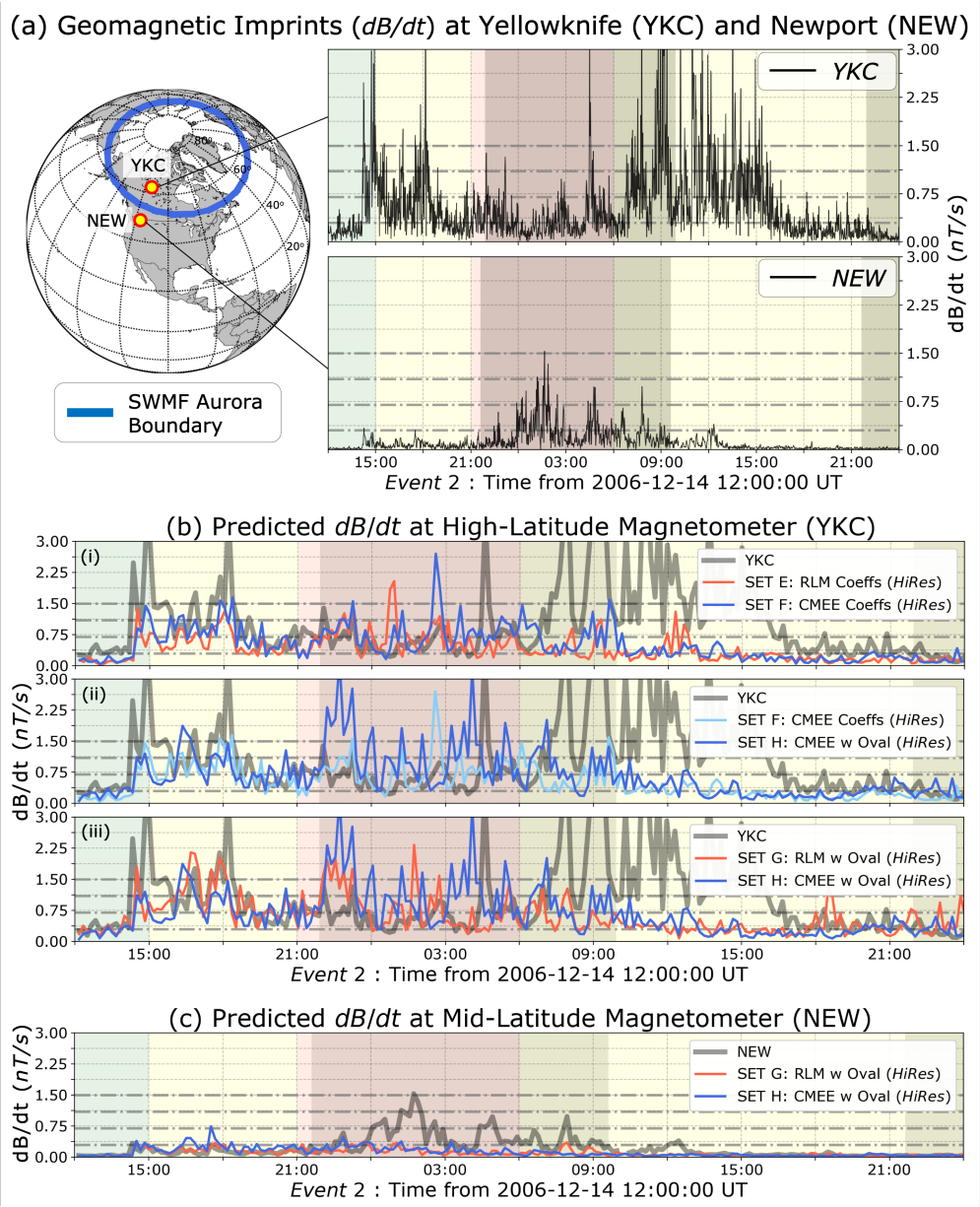

Figure 7. Impact of changes to the auroral conductance on dB/dt predictions - (a) (Left) Location of Yellowknife (YKC) and Newport (NEW) magnetometer stations mapped in geographic coordinates with the SWMF auroral boundary demarcated using the thick blue line. (Right) Raw dB/dt observations at a 1-minute cadence at YKC and NEW. (b) Comparison of max-filtered predicted dB/dt from *Hi-Res* SWMF simulations against similarly filtered dB/dt observations at Yellowknife (YKC). Goal of each panel: Top panel (i) shows impact of coefficients by comparing simulation sets E (in red) and F (in blue). Middle panel (ii) illustrates the impact of oval adjustments by comparing sets F (in light blue) and H (in blue). Bottom panel (iii) compares sets G (in red) and H (in blue). Observations are shown as a thick, grey curve. (c) Comparison of max-filtered predicted dB/dt from sets G (in red) and H (in blue) against observations (thick, grey curve). The dot-dashed lines in the line plots are markers of the thresholds used in the *Pulkkinen2013* study for their event-based analysis. The background of the line plots are coloured by Kp, similarly to Figure 5. The dark shaded background regions are times when the respective magnetometer was in the nightside.

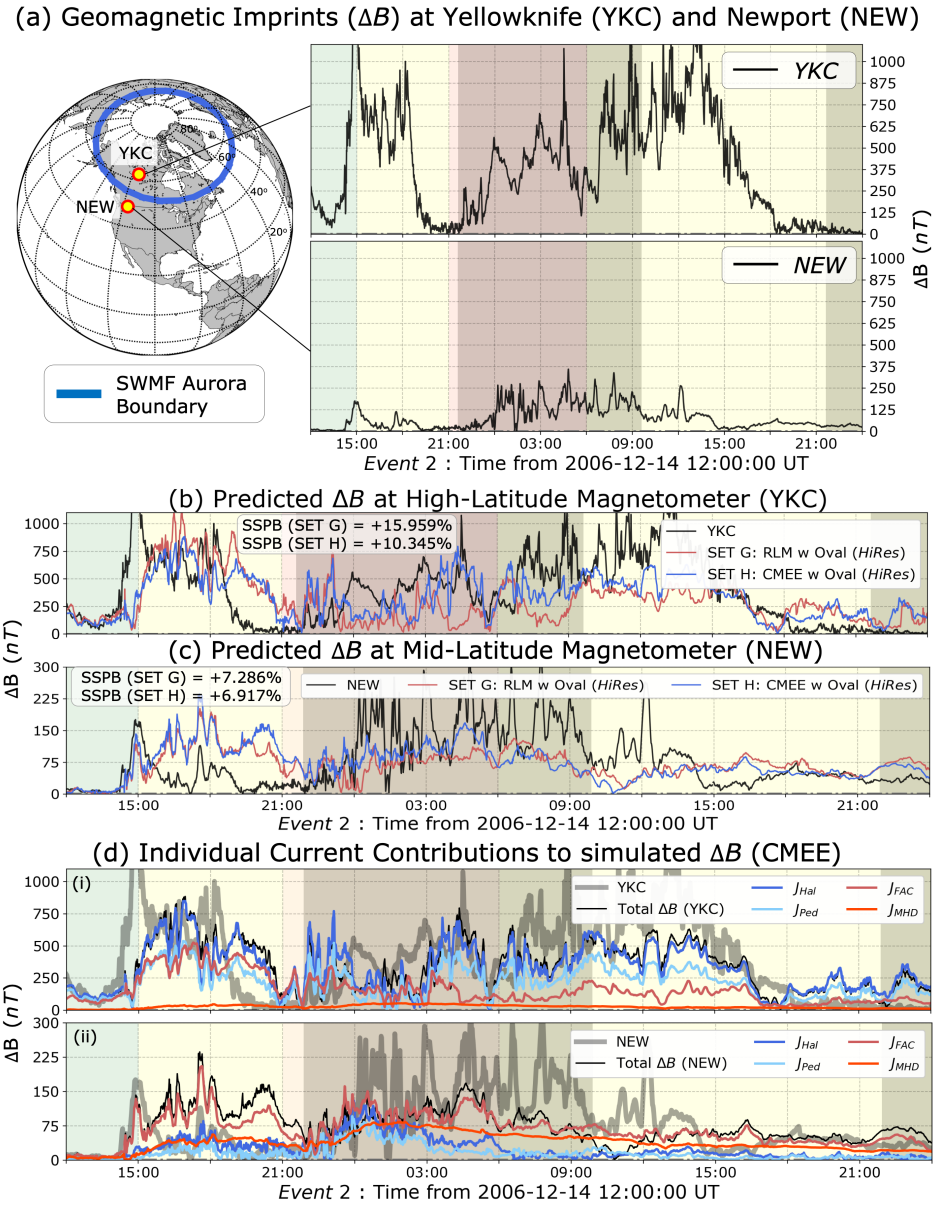

Figure 8. Impact of changes to the auroral conductance on ΔB predictions - (a) (Left) Location of Yellowknife (YKC) and Newport (NEW) magnetometer stations mapped in geographic coordinates with the SWMF auroral boundary demarcated using the thick blue line. (Right) Raw ΔB observations at a 1-minute cadence at YKC and NEW. (b) Comparison of predicted ΔB from *Hi-Res* SWMF simulations against observations at YKC, and (c) at NEW. Both subplots compare results from simulation sets G (in red) and H (in blue) against observations (in black). (d) Comparing contribution of individual current sources in the simulated ΔB at (i) YKC and (ii) NEW. The contributions from Hall currents are in blue, Pedersen currents in light blue, FACs in red, and MHD in orange. The background of the line plots are coloured by Kp, similarly to Figure 5. The dark shaded background regions are times when the respective magnetometer was in the nightside.

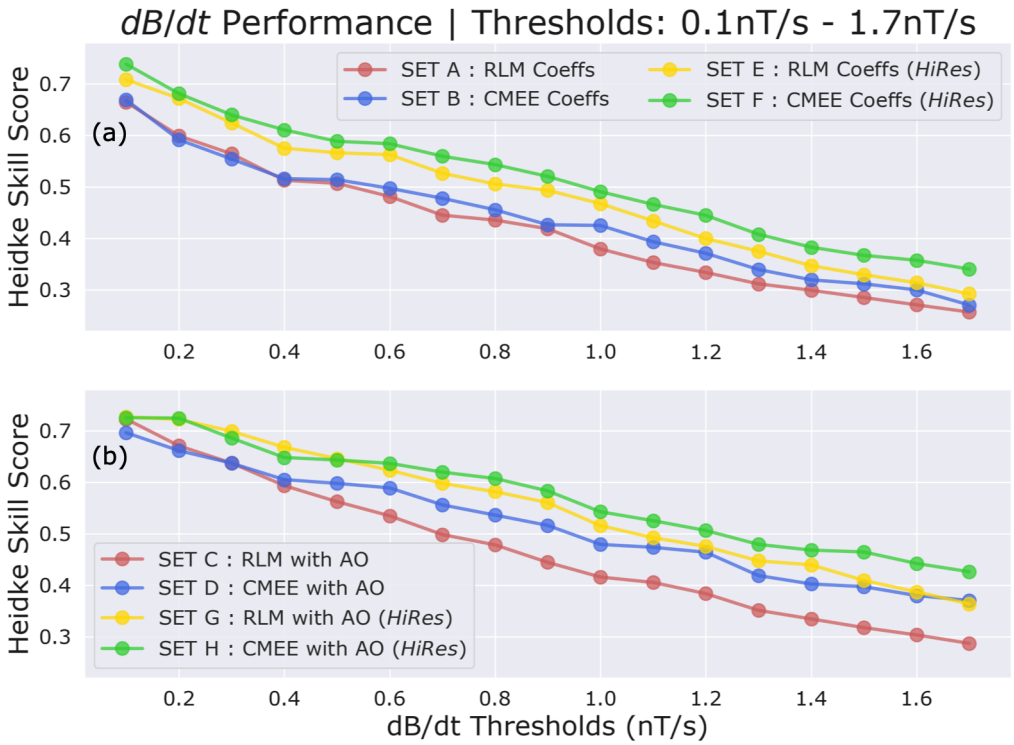

Figure 9. Heidke Skill Score (HSS) Performance of all SWMF simulation variants at ascending dB/dt predictions for all events from Table 1(a). (a) Comparison of simulation sets A (in red), B (in blue), E (in yellow) and F (in green) illustrating the impact of dataset expansion. (b) Comparison of simulation sets C (in red), D (in blue), G (in yellow) and H (in green) displaying the overall impact of dataset expansion with oval adjustments. Note the y-axis in (a) and (c) does not start at zero.

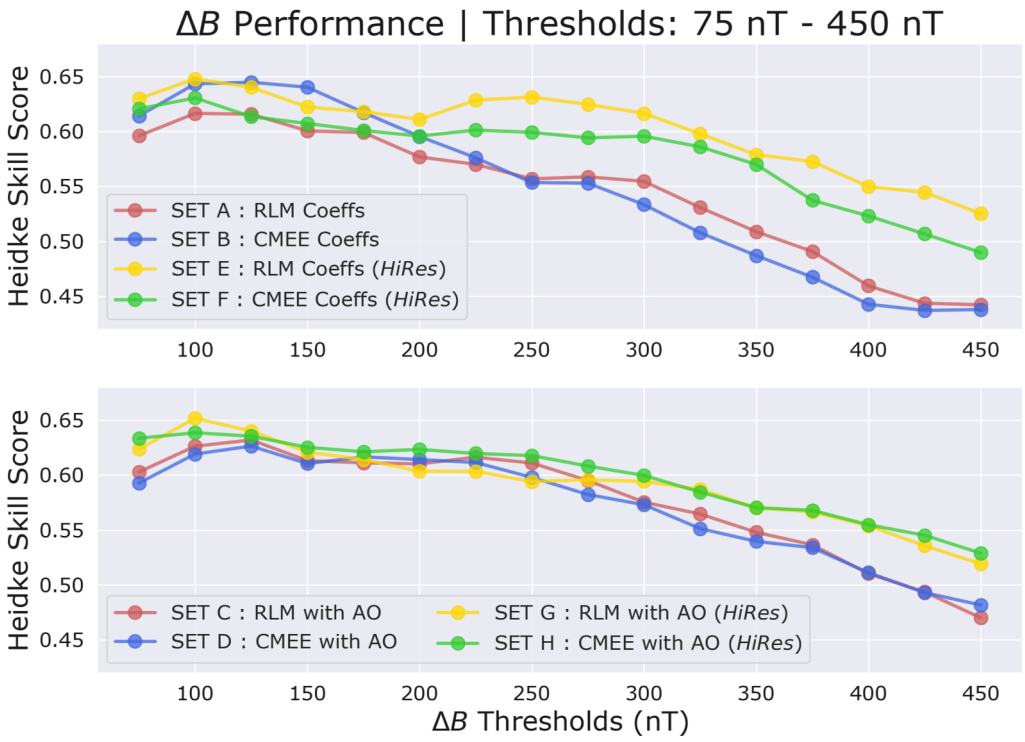

Figure 10. HSS Performance metrics of all SWMF simulation variants at ascending ΔB predictions for all events from Table 1(a). The format is similar to Figure 9. Note the y-axis in (a) and (c) does not start at zero, and spans a smaller range than Figures 9(a) and (c).

Supplementary Information for "Conductance Model for Extreme Events : Impact of Auroral Conductance on Space Weather Forecasts"

Agnit Mukhopadhyay[1], Daniel T. Welling[2], Michael W. Liemohn[1], Aaron J. Ridley[1], Shibaji Chakraborty[3], and Brian J. Anderson[4]

[1]Climate and Space Sciences and Engineering Department, University of Michigan, Ann Arbor, MI, USA
[2]Department of Physics, University of Texas at Arlington, Arlington, TX, USA
[3]Department of Electrical and Computer Engineering, Virginia Polytechnic Institute and State University, Blacksburg, VA, USA
[4]Applied Physics Laboratory, Johns Hopkins University, Baltimore, MD, USA

Corresponding author: Agnit Mukhopadhyay, agnitm@umich.edu

1 Further Investigation of Oval Expansion during *Event 2*

In Section 3.1 of the main article, Figures 7 and 8 use magnetometer measurements to assess the impact of auroral conductance on the prediction of ground-based magnetic perturbations during Event 2 that occurred on December 14 - 16, 2006. In this section, we investigate the expansion of the auroral oval using photon radiance maps from the Defence Meteorological Satellite Program's (DMSP) Special Sensor Ultraviolet Spectrographic Imager (SSUSI). In Figure 1, we display radiance dial plots at four time instances observed by the DMSP F16 satellite. Correspondingly, these time instances are marked by colour on dB/dt measurement from Yellowknife (YKC) and Newport (NEW). During the early phase of the storm, SSUSI observations at 17:38:29 UT and 22:44:17 UT show the aurora confined sharply within MLat 60^0. As the event progresses, the main phase of the storm is characterized by an expansion of the auroral oval as seen in SSUSI observations at 02:08:09 UT and 06:14:36 UT. This expansion in the auroral oval corresponds with the variation seen in the dB/dt at the latitudinally higher YKC which is within the polar cap during the main phase of the storm and observes minimal disturbances, and the latitudinally lower NEW which observes dB/dt spikes during the same period when the auroral oval expands to the lower 50s MLat.

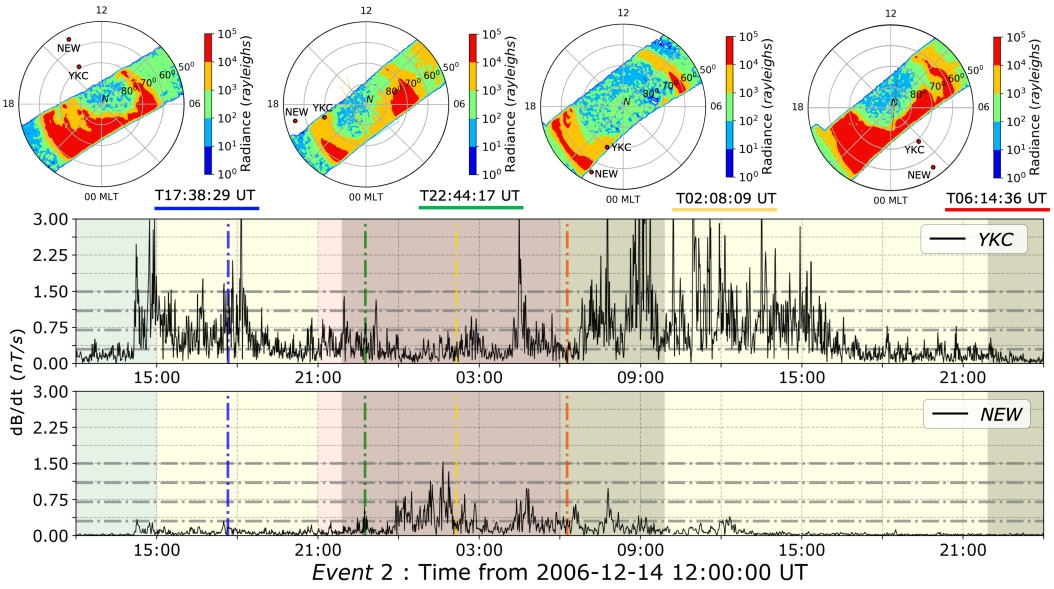

Figure 1. Expansion of the auroral oval as seen through DMSP SSUSI auroral radiance maps and the magnetometer stations at Yellowknife (YKC) and Newport (NEW). The SSUSI dial plots on top are demarcated by blue, green, yellow and red dot-dashed lines in the line plots, in increasing order of their timestamps. Line plots show raw dB/dt observations at a 1-minute cadence at YKC (top) and NEW (bottom). The background of the line plots are coloured by Kp, similarly to Figure 5 in the main paper. The dark shaded background regions are times when the respective magnetometer was on the nightside.

2 Comparison of dB/dt and ΔB Performance Metrics

The performance metrics calculated for multiple dB/dt and ΔB thresholds have been presented in the following. The metrics used has been listed in Table 2 of the main article. The format of these tables are similar to Tables 4 and 5 of the main article; for more details about those tables, please refer to Sections 3.2 and 3.3 of the main paper. For convenience, the tables have been coloured differently: In the tables listing dB/dt performance, green is used to denote best performance and red is used to denote worst. In ΔB tables, blue is used to denote best performance while orange is used to denote worst.

Usage of the auroral oval and CMEE amounts to an increase in False Negatives (F) in both ΔB and dB/dt predictions, while improving the rest of the quantities (H, M, N). Due to this reason, the FAR values are higher for oval runs, which results in less predictive score using the TSS metric. The new model (without the oval) has more misses (M) than the older model (without the oval), when predicting ΔB. For dB/dt predictions, the amount of skill lost during quieter activity, when simulating using CMEE, is more than regained with massive improvements for extreme driving, as is seen by Tables 3 to 7.

Metric	SET A	SET B	SET C	SET D	SET E	SET F	SET G	SET H
POD	0.7776	0.7801	0.8436	0.8114	0.8342	0.8555	0.8976	0.8973
POFD	0.0631	0.0615	0.0903	0.0744	0.0938	0.0892	0.1687	0.1697
FAR	0.0431	0.0419	0.0560	0.0484	0.0587	0.0547	0.0944	0.0950
MR	0.2997	0.2970	0.2367	0.2686	0.2481	0.2224	0.1817	0.1823
TS	0.7513	0.7544	0.8034	0.7793	0.7929	0.8152	0.8208	0.8201
F1	0.8580	0.8600	0.8910	0.8760	0.8845	0.8982	0.9016	0.9012
TSS	0.6572	0.6611	0.7073	0.6830	0.6932	0.7229	0.7239	0.7227
HSS	0.6645	0.6687	0.7225	0.6959	0.7080	0.7381	0.7263	0.7251

Table 1. Performance metrics table for predicted dB/dt at Threshold = **0.1 nT/s**

Metric	SET A	SET B	SET C	SET D	SET E	SET F	SET G	SET H
POD	0.5814	0.5628	0.6782	0.6638	0.6444	0.6829	0.7970	0.7979
POFD	0.0416	0.0345	0.0597	0.0477	0.0426	0.0613	0.1038	0.1164
FAR	0.0858	0.0744	0.1034	0.0861	0.0797	0.1053	0.1459	0.1606
MR	0.2499	0.2567	0.2070	0.2121	0.2207	0.2049	0.1473	0.1485
TS	0.5513	0.5384	0.6290	0.6248	0.6103	0.6321	0.7015	0.6922
F1	0.7108	0.7000	0.7723	0.7690	0.7580	0.7746	0.8246	0.8181
TSS	0.6644	0.6689	0.6896	0.7017	0.6996	0.6899	0.7068	0.6909
HSS	0.5642	0.5541	0.6370	0.6368	0.6240	0.6396	0.6987	0.6855

Table 2. Performance metrics table for predicted dB/dt at Threshold = **0.3 nT/s**

Metric	SET A	SET B	SET C	SET D	SET E	SET F	SET G	SET H
POD	0.4812	0.4840	0.5636	0.5922	0.5496	0.5989	0.7244	0.7451
POFD	0.0331	0.0302	0.0497	0.0435	0.0378	0.0543	0.0926	0.1076
FAR	0.1244	0.1138	0.1539	0.1315	0.1241	0.1576	0.2087	0.2294
MR	0.2065	0.2051	0.1821	0.1713	0.1850	0.1706	0.1284	0.1217
TS	0.4504	0.4557	0.5112	0.5434	0.5099	0.5385	0.6082	0.6098
F1	0.6211	0.6261	0.6765	0.7042	0.6754	0.7001	0.7564	0.7576
TSS	0.6692	0.6811	0.6640	0.6972	0.6909	0.6718	0.6629	0.6489
HSS	0.5069	0.5139	0.5622	0.5977	0.5661	0.5883	0.6458	0.6430

Table 3. Performance metrics table for predicted dB/dt at Threshold = **0.5 nT/s**

Metric	SET A	SET B	SET C	SET D	SET E	SET F	SET G	SET H
POD	0.3949	0.4278	0.4661	0.5305	0.4812	0.5441	0.6537	0.7057
POFD	0.0255	0.0260	0.0365	0.0387	0.0285	0.0442	0.0801	0.0936
FAR	0.1502	0.1427	0.1765	0.1667	0.1395	0.1821	0.2516	0.2667
MR	0.1847	0.1765	0.1681	0.1512	0.1630	0.1482	0.1208	0.1059
TS	0.3692	0.3994	0.4238	0.4796	0.4463	0.4853	0.5359	0.5615
F1	0.5393	0.5708	0.5953	0.6483	0.6172	0.6535	0.6978	0.7192
TSS	0.6651	0.6809	0.6553	0.6821	0.6974	0.6697	0.6277	0.6274
HSS	0.4451	0.4779	0.4983	0.5559	0.5264	0.5594	0.5975	0.6195

Table 4. Performance metrics table for predicted dB/dt at Threshold = **0.7 nT/s**

Metric	SET A	SET B	SET C	SET D	SET E	SET F	SET G	SET H
POD	0.2920	0.3310	0.3520	0.4380	0.3770	0.4440	0.5300	0.6230
POFD	0.0222	0.0235	0.0284	0.0372	0.0273	0.0434	0.0687	0.0914
FAR	0.2532	0.2408	0.2651	0.2748	0.2445	0.3041	0.3668	0.3957
MR	0.1395	0.1330	0.1299	0.1156	0.1254	0.1152	0.1015	0.0850
TS	0.2657	0.2995	0.3123	0.3756	0.3360	0.3719	0.4055	0.4425
F1	0.4198	0.4610	0.4760	0.5461	0.5030	0.5421	0.5770	0.6135
TSS	0.6073	0.6262	0.6049	0.6096	0.6301	0.5808	0.5317	0.5193
HSS	0.3533	0.3936	0.4056	0.4736	0.4341	0.4660	0.4924	0.5253

Table 5. Performance metrics table for predicted dB/dt at Threshold = **1.1 nT/s**

Metric	SET A	SET B	SET C	SET D	SET E	SET F	SET G	SET H
POD	0.2216	0.2490	0.2668	0.3557	0.2791	0.3406	0.4309	0.5554
POFD	0.0169	0.0194	0.0253	0.0319	0.0262	0.0378	0.0566	0.0784
FAR	0.3306	0.3358	0.3810	0.3674	0.3780	0.4182	0.4597	0.4775
MR	0.1089	0.1057	0.1041	0.0932	0.1026	0.0957	0.0852	0.0693
TS	0.1998	0.2211	0.2291	0.2948	0.2386	0.2736	0.3153	0.3684
F1	0.3330	0.3622	0.3728	0.4553	0.3853	0.4297	0.4795	0.5385
TSS	0.5605	0.5585	0.5150	0.5394	0.5194	0.4861	0.4551	0.4532
HSS	0.2855	0.3120	0.3179	0.3973	0.3297	0.3672	0.4094	0.4647

Table 6. Performance metrics table for predicted dB/dt at Threshold = **1.5 nT/s**

Metric	SET A	SET B	SET C	SET D	SET E	SET F	SET G	SET H
POD	0.1975	0.2070	0.2389	0.3264	0.2452	0.3153	0.3838	0.5207
POFD	0.0161	0.0155	0.0238	0.0287	0.0246	0.0356	0.0529	0.0754
FAR	0.3861	0.3659	0.4340	0.4041	0.4359	0.4649	0.5151	0.5275
MR	0.0957	0.0947	0.0919	0.0826	0.0913	0.0844	0.0779	0.0630
TS	0.1756	0.1849	0.2019	0.2673	0.2062	0.2475	0.2726	0.3293
F1	0.2988	0.3121	0.3359	0.4218	0.3418	0.3968	0.4284	0.4955
TSS	0.5181	0.5395	0.4741	0.5133	0.4728	0.4508	0.4070	0.4095
HSS	0.2573	0.2709	0.2874	0.3706	0.2926	0.3406	0.3639	0.4264

Table 7. Performance metrics table for predicted dB/dt at Threshold = **1.7 nT/s**

Metric	SET A	SET B	SET C	SET D	SET E	SET F	SET G	SET H
POD	0.7293	0.7918	0.8099	0.7879	0.8603	0.8373	0.8882	0.8740
POF	0.1882	0.2296	0.3074	0.2836	0.3388	0.3199	0.4442	0.4003
FAR	0.1013	0.1124	0.1422	0.1358	0.1467	0.1430	0.1792	0.1667
MR	0.4330	0.3823	0.3860	0.4040	0.3261	0.3540	0.3153	0.3249
TS	0.6739	0.7196	0.7140	0.7011	0.7494	0.7346	0.7439	0.7439
F1	0.8052	0.8370	0.8331	0.8243	0.8568	0.8470	0.8532	0.8532
TSS	0.4658	0.5053	0.4718	0.4602	0.5272	0.5030	0.5055	0.5085
HSS	0.4825	0.5256	0.4850	0.4772	0.5243	0.5097	0.4689	0.4891

Table 8. Performance metrics table for predicted ΔB at Threshold = **100 nT**

Metric	SET A	SET B	SET C	SET D	SET E	SET F	SET G	SET H
POD	0.6803	0.7440	0.7534	0.7460	0.8184	0.7842	0.8599	0.8432
POF	0.1186	0.1460	0.2487	0.2186	0.2743	0.2469	0.3823	0.3354
FAR	0.1166	0.1294	0.2000	0.1816	0.2025	0.1925	0.2519	0.2315
MR	0.3238	0.2836	0.3024	0.3003	0.2484	0.2745	0.2304	0.2376
TS	0.6242	0.6699	0.6340	0.6400	0.6776	0.6606	0.6668	0.6724
F1	0.7686	0.8023	0.7760	0.7805	0.8078	0.7956	0.8001	0.8041
TSS	0.5595	0.5870	0.4976	0.5181	0.5491	0.5329	0.5177	0.5309
HSS	0.5418	0.5843	0.5000	0.5200	0.5463	0.5348	0.4893	0.5158

Table 9. Performance metrics table for predicted ΔB at Threshold = **150 nT**

Metric	SET A	SET B	SET C	SET D	SET E	SET F	SET G	SET H
POD	0.6331	0.6846	0.7241	0.7128	0.7812	0.7466	0.8142	0.8045
POF	0.0711	0.1117	0.1697	0.1523	0.2059	0.1929	0.3183	0.2683
FAR	0.1107	0.1532	0.2063	0.1916	0.2263	0.2228	0.3025	0.2701
MR	0.2625	0.2424	0.2305	0.2339	0.1990	0.2206	0.1973	0.1941
TS	0.5869	0.6092	0.6093	0.6098	0.6359	0.6150	0.6017	0.6200
F1	0.7397	0.7571	0.7573	0.7576	0.7774	0.7616	0.7513	0.7654
TSS	0.6267	0.6043	0.5631	0.5744	0.5747	0.5566	0.5002	0.5358
HSS	0.5702	0.5784	0.5568	0.5638	0.5750	0.5548	0.4918	0.5335

Table 10. Performance metrics table for predicted ΔB at Threshold = **200 nT**

Metric	SET A	SET B	SET C	SET D	SET E	SET F	SET G	SET H
POD	0.5774	0.6071	0.6998	0.6692	0.7686	0.7180	0.7830	0.7887
POF	0.0527	0.0799	0.1231	0.1129	0.1504	0.1504	0.2621	0.2265
FAR	0.1208	0.1656	0.2095	0.2027	0.2277	0.2399	0.3352	0.3020
MR	0.2284	0.2208	0.1851	0.1984	0.1531	0.1805	0.1633	0.1535
TS	0.5350	0.5418	0.5903	0.5719	0.6267	0.5853	0.5613	0.5880
F1	0.6971	0.7028	0.7424	0.7277	0.7705	0.7384	0.7191	0.7406
TSS	0.6508	0.6136	0.6054	0.5989	0.6193	0.5796	0.5015	0.5445
HSS	0.5569	0.5524	0.5881	0.5717	0.6188	0.5729	0.5058	0.5502

Table 11. Performance metrics table for predicted ΔB Threshold = **250 nT**

Metric	SET A	SET B	SET C	SET D	SET E	SET F	SET G	SET H
POD	0.5553	0.5422	0.6254	0.6145	0.7021	0.6703	0.7393	0.7426
POF	0.0456	0.0562	0.0960	0.0866	0.1194	0.1229	0.2054	0.1949
FAR	0.1333	0.1624	0.2231	0.2087	0.2414	0.2555	0.3421	0.3294
MR	0.1993	0.2058	0.1812	0.1840	0.1531	0.1672	0.1491	0.1459
TS	0.5116	0.4906	0.5302	0.5287	0.5739	0.5450	0.5340	0.5441
F1	0.6769	0.6582	0.6930	0.6917	0.7292	0.7055	0.6962	0.7048
TSS	0.6674	0.6318	0.5956	0.6073	0.6055	0.5773	0.5088	0.5248
HSS	0.5562	0.5295	0.5546	0.5568	0.5930	0.5604	0.5190	0.5344

Table 12. Performance metrics table for predicted ΔB at Threshold = **300 nT**

Metric	SET A	SET B	SET C	SET D	SET E	SET F	SET G	SET H
POD	0.5076	0.4810	0.5711	0.5698	0.6345	0.6193	0.6904	0.6967
POF	0.0529	0.0507	0.0752	0.0725	0.1041	0.1052	0.1750	0.1696
FAR	0.1952	0.1970	0.2347	0.2285	0.2764	0.2834	0.3711	0.3616
MR	0.1826	0.1902	0.1662	0.1662	0.1491	0.1546	0.1389	0.1356
TS	0.4520	0.4302	0.4860	0.4875	0.5107	0.4975	0.4905	0.4995
F1	0.6226	0.6016	0.6541	0.6555	0.6761	0.6644	0.6582	0.6663
TSS	0.6222	0.6127	0.5991	0.6053	0.5744	0.5620	0.4900	0.5027
HSS	0.5082	0.4858	0.5345	0.5373	0.5497	0.5348	0.5014	0.5137

Table 13. Performance metrics table for predicted ΔB at Threshold = **350 nT**

Metric	SET A	SET B	SET C	SET D	SET E	SET F	SET G	SET H
POD	0.4602	0.4385	0.5123	0.5224	0.5687	0.5485	0.6440	0.6671
POF	0.0575	0.0523	0.0616	0.0658	0.0865	0.0901	0.1393	0.1429
FAR	0.2587	0.2500	0.2516	0.2602	0.2982	0.3146	0.3768	0.3745
MR	0.1701	0.1749	0.1568	0.1546	0.1445	0.1508	0.1289	0.1220
TS	0.3965	0.3826	0.4370	0.4413	0.4580	0.4382	0.4635	0.4767
F1	0.5679	0.5534	0.6082	0.6124	0.6283	0.6093	0.6335	0.6457
TSS	0.5712	0.5751	0.5916	0.5851	0.5573	0.5346	0.4943	0.5035
HSS	0.4585	0.4456	0.5015	0.5042	0.5135	0.4898	0.4994	0.5132

Table 14. Performance metrics table for predicted ΔB at Threshold = **400 nT**

Metric	SET A	SET B	SET C	SET D	SET E	SET F	SET G	SET H
POD	0.4211	0.4243	0.4589	0.4803	0.5230	0.4901	0.5855	0.6184
POF	0.0487	0.0482	0.0536	0.0601	0.0715	0.0690	0.1127	0.1246
FAR	0.2768	0.2732	0.2791	0.2930	0.3117	0.3181	0.3894	0.4003
MR	0.1552	0.1544	0.1472	0.1431	0.1343	0.1419	0.1236	0.1163
TS	0.3626	0.3660	0.3897	0.4005	0.4229	0.3989	0.4263	0.4377
F1	0.5322	0.5358	0.5608	0.5720	0.5944	0.5703	0.5978	0.6089
TSS	0.5680	0.5724	0.5737	0.5640	0.5541	0.5400	0.4870	0.4834
HSS	0.4360	0.4401	0.4641	0.4732	0.4928	0.4670	0.4797	0.4885

Table 15. Performance metrics table for predicted ΔB at Threshold = **450 nT**